J. Mech. Phys. Solids 151 (2021) 104384

Contents lists available at ScienceDirect

Journal of the Mechanics and Physics of Solids

journal homepage: www.elsevier.com/locate/jmps

Effect of grain orientations on fracture behavior of polycrystalline metals

Ushasi Roy, David L. McDowell, Min Zhou *

The George W. Woodruff School of Mechanical Engineering, School of Materials Science and Engineering, Georgia Institute of Technology, Atlanta, GA 30332-0405, USA

ARTICLE INFO

Keywords:
Fracture
K_{IC}, J_{IC}
Polycrystalline metals
Microstructure
Crystal plasticity

ABSTRACT

Currently no systematic approach exists to explicitly quantify the combined effects of anisotropic grain orientations and grain boundary behavior on the fracture of polycrystalline materials. A multiscale cohesive finite element (CFEM) based computational framework is developed to predict the fracture properties such as K_{IC} and J_{IC} of polycrystalline metals as functions of microstructural attributes. The focus is on characterizing the effects of crystallographic texture on fracture toughness. The framework uses computationally generated statistically equivalent microstructure sample sets with varying proportions of textured grains, allowing statistical variations and distributions of the fracture behavior due to microstructural variabilities and the influences of intergranular and transgranular fracture mechanisms to be quantified and analyzed. A crystal plasticity formulation is used to model the anisotropic deformation in the grains. A misorientation-dependent interfacial relation is used to model texture-sensitive crack growth through grains and grain boundaries. The framework allows exploration of the effects of microstructure on the macroscopic fracture measures via the manifestation of the different fracture mechanisms. Calculations carried out for Mo under 2D and a more general 2.5D plane strain conditions capture and delineate the competing effects between (a) intergranular and transgranular fracture and (b) plasticity and crack growth on the overall fracture toughness of the material. Both the 2D and 2.5D models use the same sets of microstructures; the 2.5D model uses columnar grains. The results indicate that, as the fraction of grains with preferred orientation increases, transgranular fracture dominates relative to intergranular fracture. Consequently, the relative contribution of plastic dissipation associated with transgranular fracture is enhanced, resulting in higher overall fracture toughness for the material setting analyzed. The effect is characterized in terms of the effective grain size distribution, fraction of grains with favourably oriented slip systems, and misorientation-dependent GB characteristics. Finally, an analytical correlation is established between the overall fracture resistance and the microstructure attributes.

1. Introduction

Systematic establishment of the relations between macroscale properties and microstructure attributes is important in the design of new materials with tailored properties. To understand the role of microstructure attributes such as grain orientation and grain

* Corresponding author.
E-mail address: min.zhou@gatech.edu (M. Zhou).

https://doi.org/10.1016/j.jmps.2021.104384
Received 8 September 2020; Received in revised form 29 January 2021; Accepted 26 February 2021
Available online 7 March 2021

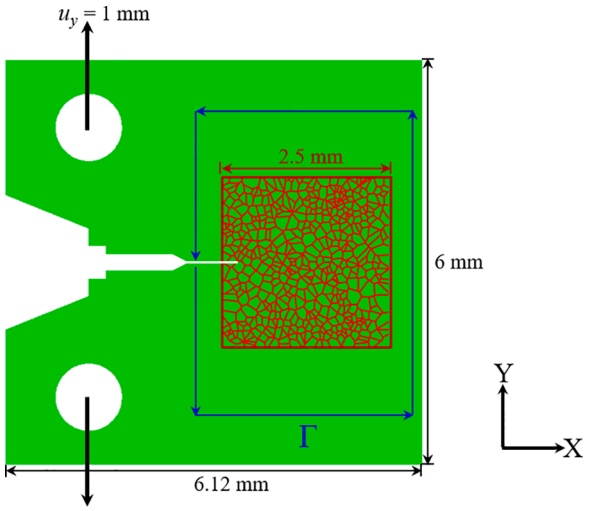

Fig. 1. Multiscale computational framework for prediction of fracture toughness of ductile metals with microstructures.

boundary (GB) characteristics on fracture, microstructure-explicit modeling of fracture processes began with the advent of computational micromechanics in mid-1980s. Asaro and colleagues (Asaro, 1983; Peirce et al., 1983; Asaro and Needleman, 1984; Deve and Asaro, 1989; McHugh et al., 1989) developed early finite element models to analyze the deformation in ductile polycrystals. Needleman and colleagues (Sham and Needleman, 1983; Christman et al., 1989; Needleman, 1992; Povirk et al., 1992) employed a finite element method to study ductile fracture by void nucleation and growth at GBs. They further extended the approach to model interfacial failure using cohesive zone methods and cohesive finite element methods (Needleman, 1992, 1993; Xu and Needleman, 1994, 1996). Based on the earlier works of Asaro, Needleman and colleagues, Zikry et al. (Zikry, 1992; Zikry and Kao, 1995, 1996; Zikry and Kameda, 1998) investigated the effects of grain orientation distribution and GB characteristics on micromechanisms of fracture using large-scale computational crystal plasticity finite element methods.

Sreeramulu et al. (2010) analyzed the effect of texture on stationary crack tip fields using crystal plasticity calculations. Kowalski et al. (2016) predicted the strain field before and after intergranular cracking in a 3D periodic polycrystalline aggregate, accounting for textured grains and cohesive interfaces along the GBs. The model does not directly concern fracture toughness or systematically delineate the effect of texture. Recently, Wilson et al. (2018) evaluated the microstructure-sensitive driving force for crack growth using discrete dislocation plasticity, crystal plasticity and extended finite element method. Even though the model considered textured polycrystalline microstructure, no direct correlation between texture and fracture was established. Simonovski and Cizelj (2015) showed that intergranular cracking in stainless steel wires is heavily influenced by texture of polycrystalline aggregates. However, the influence on fracture toughness or fracture micromechanisms was not quantified. Clayton and Knap (2016) employed phase field theory and finite element modeling to simulate the competition between fracture and twinning in both single and polycrystals. Chen et al. (2015) analyzed the effects of grain orientation and GB misorientation on fracture of polycrystals using a non-local lattice particle model. The focus was microstructure effects on crack propagation paths.

Recently, Bond and Zikry (2018) analyzed the effects of grain orientation and GB misorientation on the competition between transgranular and intergranular crack propagation. The analysis provided insights in terms of dislocation pile-ups and directional slip rates that lead to crack propagation inside the grains or along GBs. To correlate fracture toughness with microstructure attributes, Li and Zhou (2013a, 2013b, 2018) developed a cohesive finite element based multiscale model. They extented the model to 3D polycrystalline materials and adopted crystal plasticity to analyze micro fracture mechanisms (Li et al., 2014). The model assumes uniform GB properties and does not account for the effects of grain misorientations. Roy and Zhou (2020) developed a GB misorientation-dependent constitutive law and used it to analyze fracture, accounting for grain size, GB misorientation and GB strength. This work established a correlation between the fracture toughness and the grain size, grain orientation and GB characteristics, but did not consdier the anisotropic beahvior of the grains.

In addition to the computational efforts, some experimental studies (Lim and Watanabe, 1989, 1990; Watanabe, 1993, 1994, 2011; Watanabe and Tsurekawa, 1999; Kobayashi et al., 2008) have correlated fracture toughness of bicrystals with preferred grain orientations and GB misorientation. Watanabe and colleagues (Watanabe, 1993, 1994, 2011) worked extensively on GB engineering and experimentally characterized GB fracture strength as a function of the GB characteristics in different materials. In particular, they reported that the GB fracture strength in pure Mo varies in a nearly sinusoidal manner with GB misorientation angle. Arafin and Szpunar (2010) analyzed the susceptibility to intergranular cracking of Mo at different GB misorientation angles. Bachurin (2018) qualitatively correlated crack paths in polycrystalline Pd with GB misorientation. Bond and Zikry (2018), Roy and Zhou (2020) established models based on the experimental observations of Watanabe and colleagues. To date, there is no systematic characterization of the effect of grain orientation distribution on K_{IC} or J_{IC} .

In this study, we further extend the model to account for the anisotropic deformation of grains using a crystal plasticity formulation.

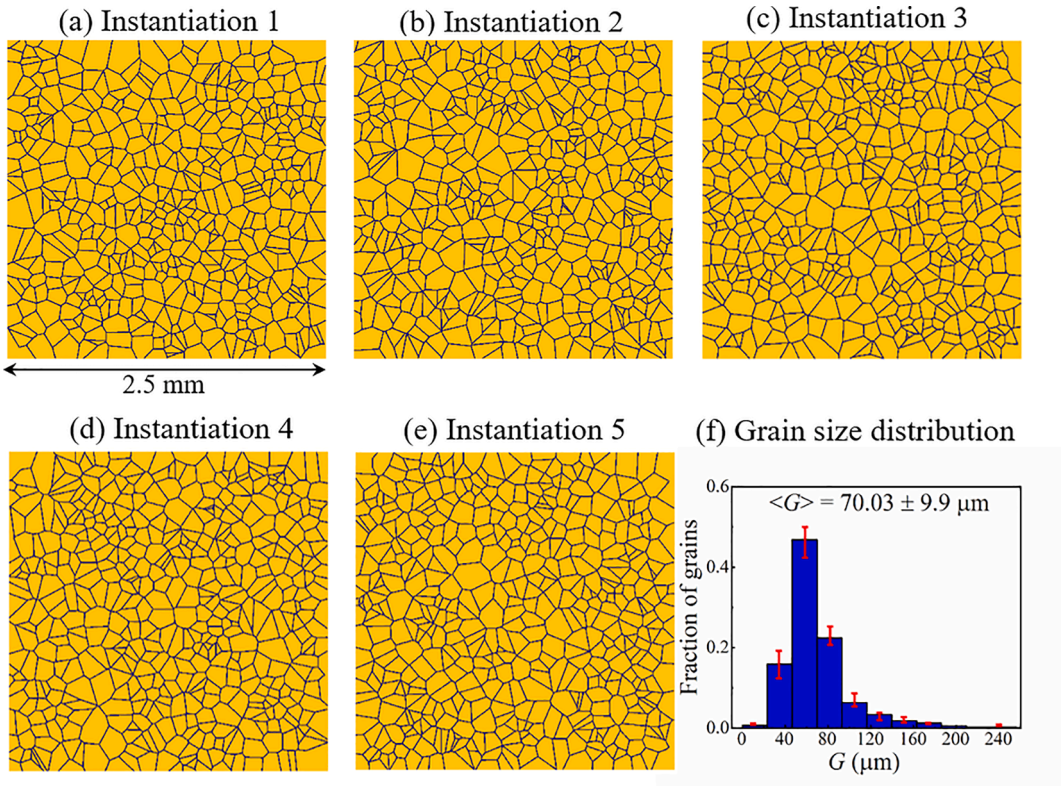

Fig. 2. (a) – (e) Computationally generated statistically similar instantiations of microstructure, (f) mean intercept grain size distribution of the microstructure set in (a–e).

The model explicitly tracks crack propagation through the polycrystalline microstructure with random and preferred grain orientations and accounts for GB misorientation. The effects of grain orientation on the competition between transgranular and intergranular ductile fracture are systematically studied. The analyses carried out focus on characterizing the K_{IC} and J_{IC} as functions of microstructural attributes that include grain size, grain orientation, GB misorientation, and GB density. Multiple statistically equivalent microstructure sample sets (SEMSS) with systematically varying attributes are used to assess the stochasticity in the fracture toughness due to microstructure heterogeneity variations. Further analyses of the results from this computational framework facilitate the development of empirical models that establish fracture toughness as function of microstructure attributes. Although the material of focus here is pure Mo, the framework and the model can be used for other materials as well.

2. Framework of analysis

2.1. Computational configuration

The primary aim is to quantitatively relate fracture toughness to microstructure attributes and the competition between different fracture mechanisms. To achieve this, it is necessary to explictly resolve microstructure-specific fracture processses. Following Roy and Zhou (2020), we adopt the cohesive finite element method (CFEM) to explicitly track transgranular and intergranular crack propagation in fully dense polycrystalline microstructures with grains and GBs. The multiscale 2D CFEM computational configuration is shown in Fig. 1. A 2D compact tension (CT) specimen is used to simulate laboratory-scale fracture toughness tests. The configuration meets all requirements of the ASTM E-1820 standard (Standard, 2001) for plane strain fracture toughness and J-integral measurements. The overall dimensions of the CT specimen are 6.12 mm × 6 mm. The region in which microstructure is explicitly modeled is 2.5 mm × 2.5 mm in size and is inserted around the tip of the pre-crack of 2.25 mm in length. The CFEM is implemented in the microstructure region which is stitched to the homogeneous region using a mesh-tie constraint, just as in Li and Zhou (2013a) and Roy and Zhou (2020). Cohesive elements are inserted along all element sides within the microstructure region and no cohesive elements are used outside this region. The size of the microstructure region is so chosen such that the plastic zone is fully contained within this region. A quasi-static boundary value problem is solved in ABAQUS/Standard in conjunction with an UMAT using the modified Newton's technique for non-linear equations. Overall Mode-I loading is imposed via load point displacement, as indicated in Fig. 1. Load point displacements are specified with general multiple point constraint (MPC) on the surface of the hole. All nodes on the circumference of the hole in 2D is kinematically coupled with the rigid body motion of the reference point (load point) in the Y direction. Therefore, plastic straining around the hole is negligible. The edges of the specimen are traction-free and conditions of plane

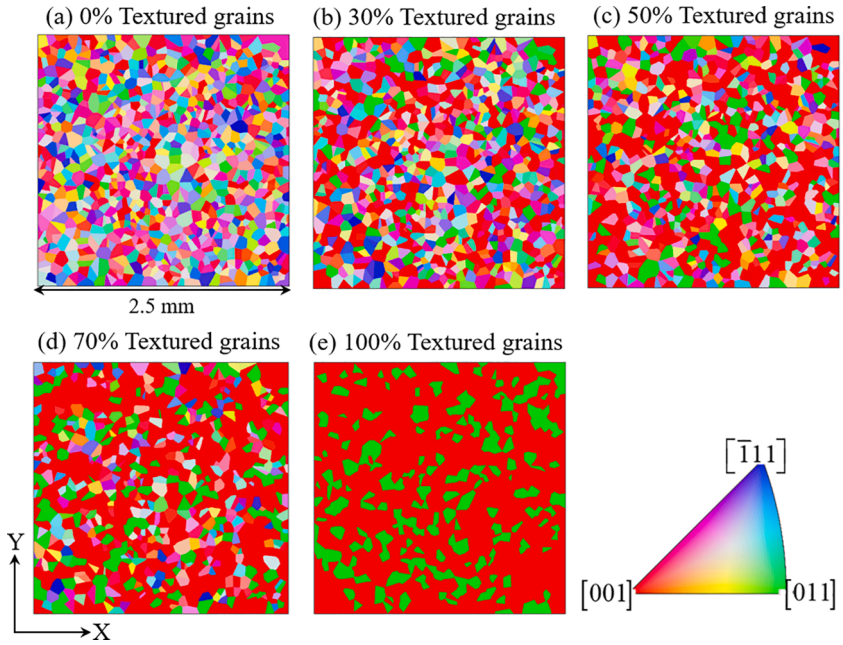

Fig. 3. One out of five instantiations of microstructure from each of the five statistically equivalent microstructure sample sets (SEMSS). The colors in the stereographic triangle indicate the crystalline plane normals of grains parallel to the XY plane normal of the specimen in Fig. 1.

strain are imposed.

2.2. Material and microstructure

To account for the effect of grain orientation distribution and GB characteristics on the fracture of polycrystalline ductile materials, single phase pure molybdenum (Mo) is chosen since significant experimental data exist (Lim and Watanabe, 1989, 1990; Watanabe, 1993, 1994, 2011). Specifically, the data for pure Mo (Watanabe, 2011) show that GB fracture strength exhibits a near sinusoidal variation with the GB misorientation angle. GBs with misorientation angle below 15° or above 75° are nearly as strong as the grains, but GBs with misorientation angles in the range of 15° - 75° can have strengths as low as half of that of the grains. These low fracture strength GBs are preferred sites for crack formation and propagation.

First, 2D microstructures with random grain morphologies are generated using the Voronoi tessellation function. A set of five statistically similar instantiations so generated are shown in Fig. 2 along with their grain size distribution. These instantiations are similar in terms of their mean intercept grain size distribution and the average grain size (~70 μm with a standard deviation of 9.9 μm). The error bars denote the variations among the samples in the set. The set of Euler angles (Φ_1, Φ, Φ_2) is used to specify the 3D orientation of each grain in the 2D microstructure with respect to the specimen axes, as indicated in Fig. 1. 3D orientations are phenomenologically assigned to the 2D microstructures. In order to systematically study the effect of crystallographic texture, grains are initially assigned orientations following two specific orientation distributions, as quantified by the orientation distribution function (ODF). These distributions have preferred orientations along the {011}<211> and the {110}<001> texture components with varying degrees of deviation from the preferred texture components. The resulting orientation distributions are shown in Appendix A with the colors representing orientations in the included pole figure. A total of $4 \times 2 = 8$ statistically equivalent microstructure sample sets are generated, each containing five statistically similar instantiations or samples. The instantiations are statistically similar in terms of both texture (as measured by the ODF) and microstructure morphology (as measured by the grain size distributions). The details of the microstructures and their (011) pole figures are given as supplementary information in Appendix A. Together with the approach for predicting the fracture toughness described in the following sections, these systematic variation of the texture allows the effect, or the lack of the effect, of the statistical nature of grain orientations on fracture toughness to be analyzed and quantified. As it will be seen later, the fracture toughness exhibits negligible dependence on texture over the range analyzed here. This can be attributed to the fact that these changes in the texture do not lead to significant changes in the statistical distribution of the GB misorientation angle which is the primary factor affecting fracture behavior. More specifically, the changes in grain orientation distribution do not give rise to significant amounts of low-strength high angle GBs which govern the crack path and, consequently, fracture toughness. The details are provided in Appendix A. In order to gain more insights on how grain orientations influence fracture, microstructures with different effective grain sizes are designed with a view to influence GB misorientations, as described below.

To delineate the effect of crystallographic texture, the microstructures are designed to contain prescribed proportions of textured grains (TG) and randomly oriented grains. Each instantiation in the five microstructure sample sets with statistically equivalent random grain morphologies shown in Fig. 2 is assigned five texture levels (0%, 30%, 50%, 70%, and 100%). Each microstructure

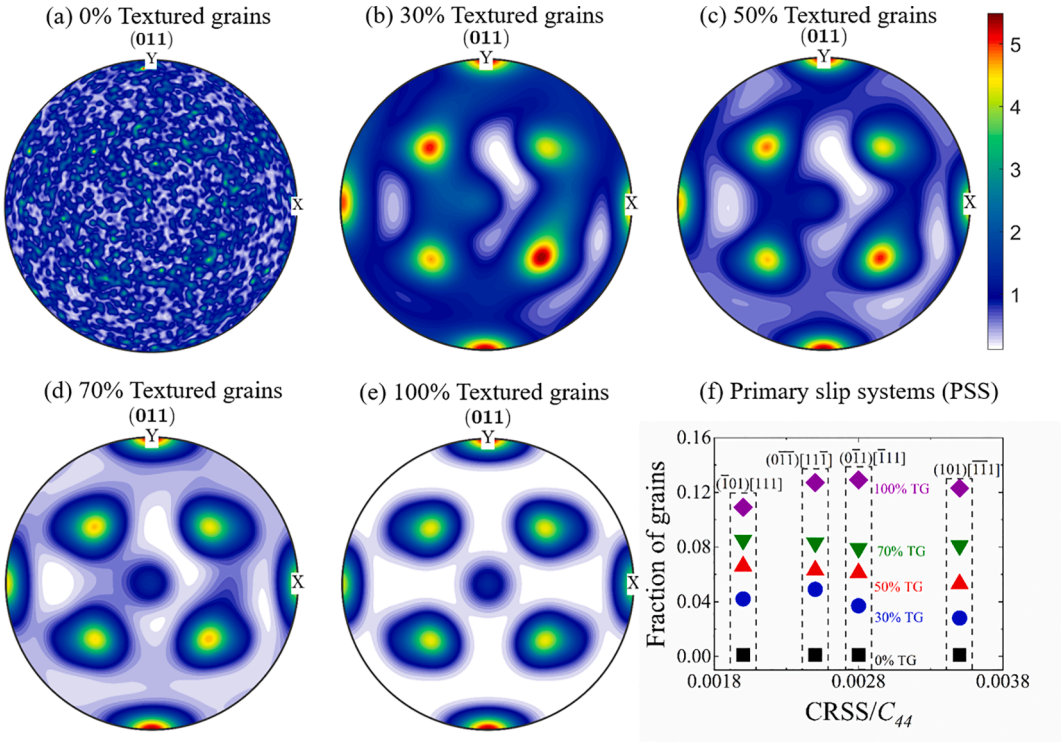

Fig. 4. (a) – (e) (011) pole Figures showing the orientation distribution functions of the five SEMSS. The colors represent intensity of a particular orientation measured in arbitrary units. (f) fraction of grains with favorably orientated primary slip systems as a function of the critical resolved shear stress (CRSS) normalized by the C_{44}.

sample set contains five statistically similar instantiations. The base case has no (0%) TG, i.e., all grains are randomly orientated. The other four sets have 30%, 50%, 70%, and 100% TG, respectively. The preferred orientation targets are characterized by two texture components, i.e., the rotated cubic component and the Goss component. Multiple texture components are observed in Mo due to different processing routes and deformation modes such as hot rolling, cold rolling, and shearing. Some of these texture components remain in the recrystallized microstructure after annealing. The rotated cubic component {001}<110> is the most common type (Chen et al., 2013, 2014; Lobanov et al., 2016; Oertel et al., 2010; Primig et al., 2015; Welch and Davies, 1983). The Goss component {011}<100> preferably aligns the primary slip systems with the X-Y plane of the specimen. This facilitates enhanced plasticity in the grains and thus magnifies the competition between plasticity and new surface creation. The statistically equivalent microstructure sample set with 100% TG contains ~25% {001}<110> texture components and ~75% {011}<100> components. This ratio of the two texture components holds in the three partially textured sample sets as well. The 100% TG closely resembles the limiting case of a bi-crystal specimen in which each grain is oriented along either the {001}<110> or the {011}<100> orientation with respect to the specimen axes shown in Fig. 1. The statistical equivalence among the five samples in each set is in terms of grain size distribution, grain morphology, and the fraction of TG. Fig. 3 shows one microstructure sample (one representative instantiation) from the statistically equivalent microstructure sample sets at each texture level. The grain orientations are denoted by the plane of the grains that is parallel to the specimen plane (X-Y) using the scheme of plane colors in the stereographic projections of the crystallographic plane normals on an inverse pole figure map Nolze and Hielscher (2016) with misorientation tolerance level of 5°. The misorientation tolerance is discussed in the next paragraph. Due to crystallographic symmetry, the standard stereographic triangle contains all possible grain orientation relations. The distributions of grain orientations are shown using (011) pole figures (Fig. 4). The microstructure in Fig. 3(e) exhibits clearly the {001}<110> and {011}<100> texture components seen in the (011) pole figure in Fig. 4(e). As the fraction of TG decreases, the intensity of the texture components decreases and the pole figure eventually depicts no orientation preference (Fig. 4 (a)). The grains with preferred orientations have the primary slip systems (PSS) favorably aligned for easier activation of slip. Different orientations facilitate favorable alignment of some of the four primary slip systems of Mo. Fig. 4(f) shows the fraction of the grains with favorably oriented primary slip systems. These slip systems could be ranked in terms of their critical resolved shear stress (CRSS). The figure shows the fractions as a function of the CRSS/C_{44} (see below about C_{44}). Lower values of CRSS/C_{44} denote easier slip activation. As expected, the fraction of grains with favorably oriented PSS increases as the faction of the TG increases.

Although the internal grain structure remains the same for all the statistically equivalent microstructure sample sets, an effective grain size distribution arises after assignment of the crystallographic texture from the viewpoint of misorientation. An effective grain size is defined as the maximum microstructural unit along which a straight crack can propagate in an uninterrupted manner (Ghosh et al., 2016; Kim et al., 2000, 2003). Usually, this effective grain size is experimentally measured using EBSD analysis. A tolerance limit

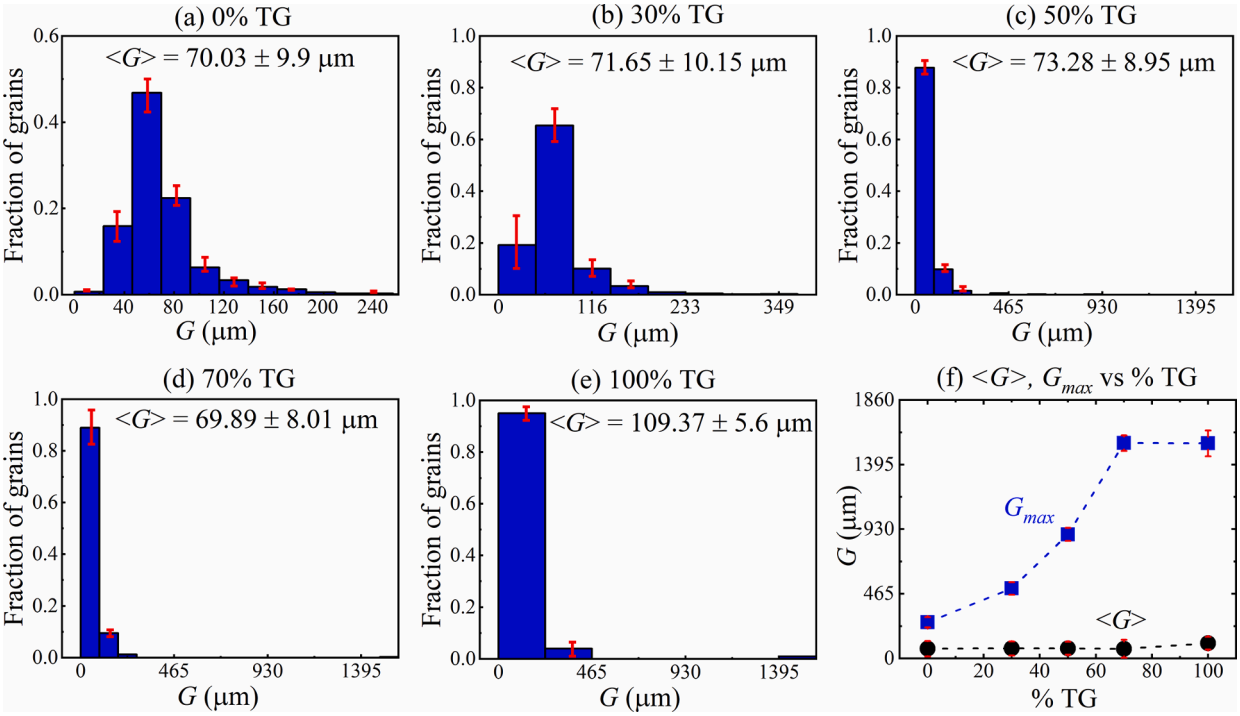

Fig. 5. (a) – (e) effective grain size distributions for the five SEMSS, and (f) maximum effective grain size and the mean effective grain size as functions of the fraction of textured grains (TG).

on the GB misorientation is set to determine the effective grain size based on the concept that a transgranular cleavage crack changes its course when it encounters a high angle boundary. Low angle boundaries are known to have higher fracture resistance. This is also the case for Mo, as described by Watanabe (1993). We define the effective grain size with a tolerance of 5° for our cases. This means if the misorientation between two adjacent grains lies within 5°, the two grains are considered to be one since the crack path is not hindered by such a low angle GB. The effective grain size distributions are shown in Fig. 5(a–e). The error bars show the range of variations among the five samples in the statistically equivalent microstructure sample sets. Since random orientations are assigned to the grains in case of the set with 0% TG, the distribution is nearly symmetric and monomodal and is the same as shown in Fig. 2(e). As the fraction of TG increases, the distribution changes progressively, showing higher fractions of grains with finer effective grain sizes and a few grains with much larger effective sizes (Fig. 5(d–e)). It is to be noted that the number of effective grains decreases as the amount of TG increases, resulting in higher fractions of smaller grains. Fig. 5(f) shows that the mean effective grain size $\langle G \rangle$ remains nearly constant as the fraction of TG increases. However, the maximum value of the effective grain size $G_{\max}$ increases as the fraction of TG increases, accounting for the large fraction of grains oriented along/nearly along the {110}<100> direction with a misorientation tolerance of 5°. Henceforth, the effective grain size defined with a 5°of tolerance on misorientation is used as the measure for grain size, unless otherwise specified.

The GB misorientation is characterized by the minimum angle by which one grain is to be rotated about an axis common to the contacting grain pair in order to bring the grains into coincidence. The Euler angle sets are used to calculate the orientation matrix (g) for all grains. This matrix is

$$g = \begin{bmatrix} \cos\Phi_1\cos\Phi_2 - \sin\Phi_1\sin\Phi_2\cos\Phi & \sin\Phi_1\cos\Phi_2 + \cos\Phi_1\sin\Phi_2\cos\Phi & \sin\Phi_2\sin\Phi \\ -\cos\Phi_1\sin\Phi_2 - \sin\Phi_1\cos\Phi_2\cos\Phi & -\sin\Phi_1\sin\Phi_2 + \cos\Phi_1\cos\Phi_2\cos\Phi & \cos\Phi_2\sin\Phi \\ \sin\Phi_1\sin\Phi & -\cos\Phi_1\sin\Phi & \cos\Phi \end{bmatrix}. \quad (1)$$

The misorientation matrix (Δg) at the GBs is calculated via

$$\Delta g = g_1 . g_2^{-1}, \quad (2)$$

where g_1 and g_2 are the orientation matrices of the two neighboring grains. The misorientation angle (θ) is then calculated using the trace of the misorientation matrix via

$$\cos\theta = \frac{1}{2}[trace(\Delta g)]. \quad (3)$$

The axis of misorientation can be calculated using the off-diagonal terms of the misorientation matrices. Since our focus is on resolving the fracture behavior of GBs as a function of misorientation angles, the misorientation axes are not shown. Fig. 6 shows the

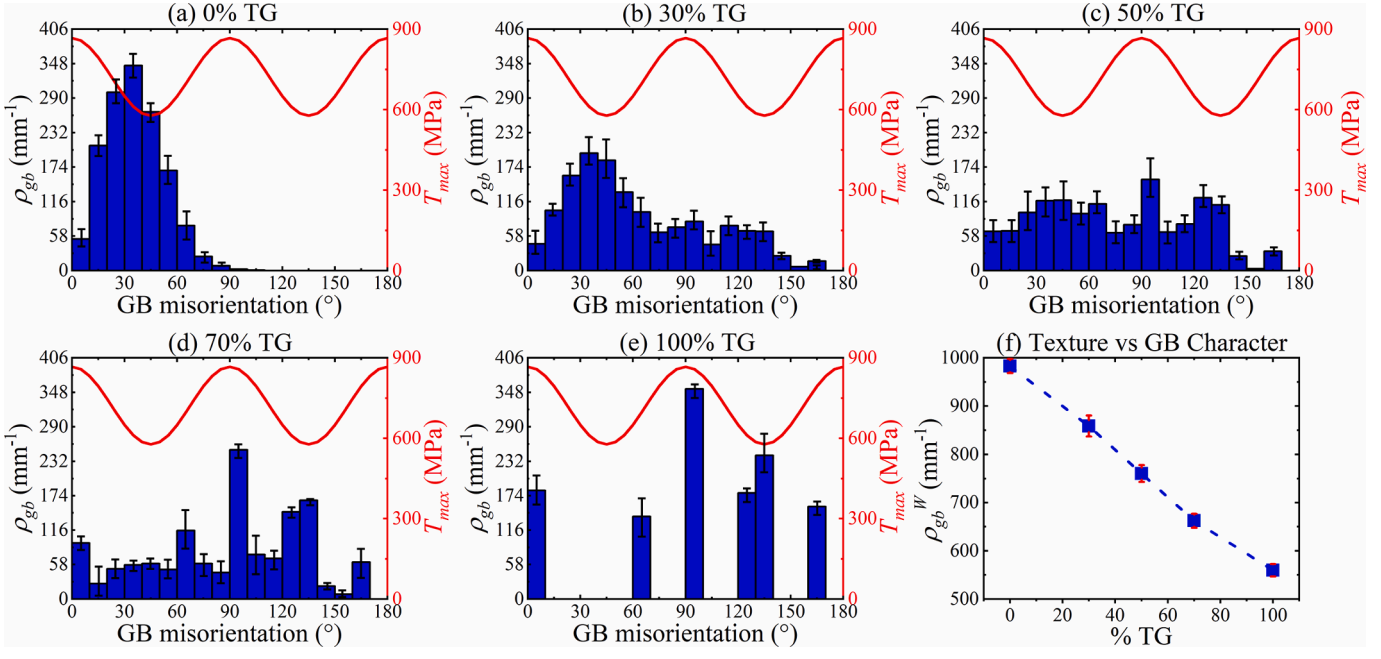

Fig. 6. (a) – (e) distributions of grain boundary misorientation angles for the five SEMSS. The GB fracture strength as a function of the misorientation angle is also shown. (f) density of weaker GBs as a function of the fraction of textured grains (TG).

misorientation angle distributions for the five microstructure sets. The GB density (ρ_{gb}) is defined as,

$$\rho_{gb} = \frac{L_{gb}}{A_m}, \tag{4}$$

where L_{gb} denotes the total length of the GBs, and A_m denotes the area of the microstructure region. The GBs with misorientation angles in the range of $15^\circ - 75^\circ$ or $135^\circ - 155^\circ$ are the fracture prone sites in a polycrystalline material and are hence referred to as the weaker GBs with an associated density of ρ_{gb}^W. The distributions of the misorientation angle over the entire range of the misorientation angle and the GB fracture strength as a function of the misorientation angle are both shown in Fig. 6(a)–(e). For the five statistically equivalent microstructure sample sets, overall, the density of weaker GBs decreases as the fraction of TG increases (see Fig. 6(f)).

2.3. Material models

The primary goal is to characterize the effects of grain orientation (texture) and GB misorientation on crack path and, through the analysis, quantify the relative contributions of transgranular and intergranular fracture on overall fracture resistance. To focus on the effect of grain orientation on the competition between crack growth and plastic deformation, a crystal plasticity formulation is used for the grains. To account for the effect of GB misorientation, a misorientation angle dependent interfacial law is used for the GBs. A simple isotropic elastic-plastic law is adopted for the homogenized section of the specimen outside the microstructure region (Fig. 1).

2.3.1. Crystal plasticity formulation

Plastic deformation in metals is a manifestation of dislocation motion and interaction at the microscopic scale. The details are intimately related to the crystallographic structure of the material as well as the current state of the microstructure. Macroscopic models of plasticity lack the ability to link these fundamental mechanisms to the bulk material response without very substantial experimental characterization. Many formulations of constitutive laws for the elastic-plastic deformation of single and polycrystals have long been proposed (Taylor, 1938; Hill and Rice, 1972; Asaro and Rice, 1977; Peirce et al., 1982; McGinty and McDowell, 2004). The basic premise of these theories is that macroscopic plastic deformation is related to the cumulative process of slip system shearing relative to the lattice. This methodology provides a physical link between the processes at different length scales. The two basic components of crystal plasticity model are the kinematic and kinetic relations.

The multiplicative decomposition of the total deformation gradient is given by

$$\mathbf{F} = \mathbf{F}^e \cdot \mathbf{F}^p, \tag{5}$$

where $\mathbf{F}^e$ is the elastic deformation gradient representing the elastic stretch and rotation of lattice, and $\mathbf{F}^p$ is the plastic deformation gradient describing the collective effects of dislocation motion along the active slip planes relative to a fixed lattice in the reference configuration. Unit vectors $\boldsymbol{s}_0^\alpha$ and $\boldsymbol{n}_0^\alpha$ denote the slip direction and the slip plane normal direction, respectively, for the α^{th} slip system in the undeformed configuration. For Mo with bcc crystal structure, 24 slip systems of {110}<111> type are considered since the experimental works suggest that almost under all circumstances, activation of the {110}<112> type slip systems is rather rare (Kim and Greer, 2008; Gröger and Vitek, 2009; Kim et al., 2010, 2012).

The resolved shear stress on each slip system is related to the Cauchy stress tensor σ according to

$$\tau^\alpha = \boldsymbol{\sigma} : (\boldsymbol{s}^\alpha \otimes \boldsymbol{n}^\alpha), \tag{6}$$

where the slip vectors have been rotated into the current configuration. Under the application of the resolved shear stress, the slip system shearing rates $\dot{\gamma}^\alpha$ on the slip systems are related to the plastic velocity gradient ($\mathbf{L}^p$) in the isoclinic intermediate configuration according to

$$\mathbf{L}^p = \sum_\alpha \dot{\gamma}^\alpha \boldsymbol{s}_0^\alpha \otimes \boldsymbol{n}_0^\alpha, \tag{7}$$

with $\dot{\gamma}^\alpha$ being prescribed to follow the rate-dependent flow rule

$$\dot{\gamma}^\alpha = \dot{\gamma}_0 \left\langle \frac{\tau^\alpha - \chi^\alpha}{g^\alpha} \right\rangle^m \mathbf{sgn}(\tau^\alpha - \chi^\alpha). \tag{8}$$

Here, m is the inverse strain rate sensitivity exponent, and g^α and χ^α are drag stress and back stress, respectively, on the α^{th} slip system. These quantities evolve according to

$$\left.\begin{aligned} \dot{g}^\alpha &= H \sum_{\beta=1} q^{\alpha\beta} |\dot{\gamma}^\beta|, \text{ and} \\ \dot{\chi}^\alpha &= A_{kin} \dot{\gamma}^\alpha - A_{dyn} \chi^\alpha |\dot{\gamma}^\alpha|. \end{aligned}\right\} \tag{9}$$

In the above relations, $q^{\alpha\beta}$ is the latent hardening coefficient, H, A_{kin} and A_{dyn} are the isotropic hardening, kinematic hardening and dynamic recovery coefficients, respectively.

Also, for bcc crystals, the dislocation core spreads onto multiple planes, giving rise to twinning-anti-twinning asymmetry in yielding. The criterion for yielding thus considers two shear stresses parallel and two shear stresses perpendicular to the slip direction,

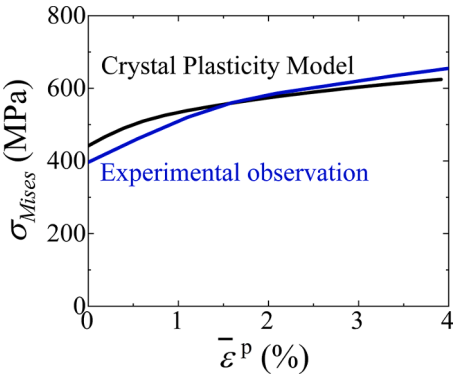

Fig. 7. Comparison of the Mises effective stress – plastic strain response calculated from the 2D crystal plasticity model with experimental observation as reported in Sturm et al. (2007).

Table 1
Parameters of the 2D crystal plasticity model.

$\dot{\gamma}_0$ (s^{-1})	m	A_{kin} (MPa)	A_{dyn}	H (MPa)	$q^{\alpha\beta}$	a_1	a_2	a_3
0.1	13	8	400	65	1	0.24	0.35	0

both resolved in two different {110} planes of the zone of the slip direction. For the [111] slip direction, such a yield criterion is expressed as (Gröger and Vitek, 2009),

$$\sigma^{(\bar{1}01)} + a_1\sigma^{(0\bar{1}1)} + a_2\tau^{(\bar{1}01)} + a_3\tau^{(0\bar{1}1)} = \tau_{CRSS}^{(0\bar{1}1)[111]}, \tag{10}$$

where $\sigma^{\{110\}}$ and $\tau^{\{110\}}$ are the shear stresses parallel and perpendicular to the slip direction, respectively, in the corresponding {110} planes. The first term in the above equation is the Schmid stress that drives the dislocation motion in the glide plane and does work through the glide. The last three terms are the non-Schmid stresses that affect the restriction of the dislocation core but do not do any work as the dislocation glides. The values of the coefficients a_1, a_2, and a_3 are taken from Gröger and Vitek (2009). These non-linear coupled differential equations are solved using a UMAT in ABAQUS.

The elastic part of the behavior of the grains is orthotropic in the rate form. Specifically, the Jaumann rate of Kirchhoff stress ($\dot{\boldsymbol{\tau}}$) evolves with the rate of deformation tensor ($\mathbf{D}$) following

$$\dot{\boldsymbol{\tau}} = \mathbf{C} : (\mathbf{D} - \mathbf{D}^{p}), \tag{11}$$

where $\mathbf{C}$ represents the fourth-order tensor of elastic moduli which, in the Voigt notation, takes the form of

$$C = \begin{bmatrix} C_{11} & C_{12} & C_{13} & 0 & 0 & 0 \\ & C_{22} & C_{23} & 0 & 0 & 0 \\ & & C_{33} & 0 & 0 & 0 \\ & & & C_{44} & 0 & 0 \\ & Sym & & & C_{55} & 0 \\ & & & & & C_{66} \end{bmatrix}. \tag{12}$$

In this paper, the otherwise 3D constitutive model is effectively constrained to model 2D (plane strain) behavior. A single slip model is assumed for the 2D grains. As such, cross-slip within a single grain is neglected. The phenomenologically assigned 3D orientations of the grains are first used to identify the orientation of the slip systems with respect to the XY plane of the 2D specimen (Fig. 1). A slip system is assigned its appropriate CRSS value as given in Fig. 4(f) only if the corresponding slip direction (a) lies on or (b) nearly (deviation within $\sim\pm 1^{\circ}$) of lying within the 2D plane of the specimen. By this definition, slip can potentially be activated on the α^{th} slip system only if the scalar projection of the slip direction on the (001) unit normal to the XY plane of the 2D case in a global coordinate system is very small, i.e., $s_g^{\alpha} \cdot (001) \in [-0.0175, 0.0175]$. Here, s_g^{α} denotes the unit vector in the slip direction of the α^{th} slip system in the global coordinate system. Any slip system that does not satisfy this criterion is assigned a CRSS one order of magnitude higher than the actual CRSS value of that particular slip system to impose this constraint. This ensures that slip systems with slip directions effectively lying out of the 2D plane are never activated. Fig. 7 shows the effective stress-strain curve obtained using these constraints for a 2D microstructure with randomly oriented grains (no texture) under plane strain conditions. This figure illustrates that parameters of the constitutive model can be selected to conform to the experimentally measured stress-strain curve Sturm et al. (2007). Material parameters used in the crystal plasticity model are shown in Table 1.

Table 2
Parameters of the elastic-plastic model.

C_{11} (MPa)	C_{12} (MPa)	C_{44} (MPa)	ν	σ_y(MPa)	k (MPa)
449,970	172,870	124,970	0.38	385	13,700

2.3.2. *Isotropic model for the homogenized region*

The homogenized region outside the microstructure region follows a rate-independent elasto-plastic constitutive law with isotropic hardening under the large strain assumption. An incremental theory of plasticity is used. For the linear elastic response, the Jaumann rate of Kirchhoff stress ($\boldsymbol{\tau}$) evolves with the elastic part of the rate of deformation tensor ($\mathbf{D}$) following Eq. (11). For the isotropic elastic response, $\mathbf{C}$ in Eq. (11) is given by

$$\mathbf{C} = 2\overline{\mu}\widetilde{\mathbf{I}} + \overline{\lambda}\mathbf{I} \otimes \mathbf{I}, \tag{13}$$

where,

$$\overline{\lambda} = \frac{\overline{E}\overline{\nu}}{(1+\overline{\nu})(1-2\overline{\nu})}, \text{ and } \overline{\mu} = \frac{\overline{E}}{2(1+\overline{\nu})}. \tag{14}$$

In the above relations, $\widetilde{\mathbf{I}}$ is the fourth-order identity tensor, $\mathbf{I}$ is the second-order identity tensor, $\overline{E}$ is the effective elastic modulus, $\overline{\nu}$ is the effective Poisson's ratio, and $\otimes$ denotes the fourth-order tensor product of two tensors. The effective elastic constants for the homogenized region are calculated using the self-consistent method as Sisodia and Verma (1990), i.e.,

$$\left.\begin{aligned} \overline{G} &= \frac{4(C_{11}-C_{13})+2(C_{33}-C_{12})+6(C_{66}+2C_{44})}{60} + \\ &\frac{15}{4}\left\{\frac{2(C_{11}+C_{12})+C_{33}+4C_{13}}{(C_{11}+C_{12})C_{33}-2C_{13}^2} + \frac{3}{C_{11}-C_{12}} + \frac{1.5}{C_{66}} + \frac{3}{C_{44}}\right\}^{-1}, \\ \overline{B} &= \frac{1}{18}(2C_{11}+C_{33}+2C_{12}+4C_{13}) + \frac{C_{33}(C_{11}+C_{12})-2C_{13}^2}{2(C_{11}+C_{12}+C_{33}+4C_{13})}, \\ \overline{E} &= \frac{9\overline{B}\overline{G}}{3\overline{B}+\overline{G}}, \quad \text{and} \quad \overline{\nu} = \frac{3\overline{B}-2\overline{G}}{6\overline{B}+2\overline{G}}. \end{aligned}\right\} \tag{15}$$

Where $\overline{G}$, and $\overline{B}$ represent the effective shear, and bulk modulus of the polycrystalline aggregate respectively. The magnitudes of all these elastic constants are taken from Featherston and Neighbours (1963). All relevant material parameters are listed in Table 2.

The rate of deformation tensor is decomposed into an elastic part and a plastic part, i.e.,

$$\mathbf{D} = \mathbf{D}^e + \mathbf{D}^p. \tag{16}$$

The plastic part of $\mathbf{D}$ varies with the deviatoric part of the Kirchhoff stress, i.e.,

$$\left.\begin{aligned} \mathbf{D}^P &= \frac{3\dot{\overline{\varepsilon}}^p}{2\overline{\sigma}}\boldsymbol{\tau}', \text{ where,} \\ \overline{\sigma} &= \sqrt{\frac{3}{2}\boldsymbol{\tau}' : \boldsymbol{\tau}'}, \text{ and} \\ \dot{\overline{\varepsilon}}^p &= \frac{1}{k}\left\langle \frac{3\boldsymbol{\tau}'}{2\overline{\sigma}} : \dot{\boldsymbol{\tau}} \right\rangle \frac{3\boldsymbol{\tau}'}{2\overline{\sigma}}. \end{aligned}\right\} \tag{17}$$

Here, $\overline{\sigma}$ is the uniaxial equivalent stress, $\dot{\overline{\varepsilon}}^p$ is the equivalent plastic strain rate which takes non-zero values only after yielding, and $\boldsymbol{\tau}'$ is the deviatoric part of Kirchhoff stress $\boldsymbol{\tau}$. The material follows the Mises flow rule with isotropic hardening characterized by k in the above equation. The constitutive relation used is the bilinear stress-strain relation under uniaxial loading, with the part after yielding being in the form of

$$\overline{\sigma} = \sigma_y + k\overline{\varepsilon}^p, \tag{18}$$

where, σ_y is the Mises yield stress that corresponds to the yield strength estimated from uniaxial tensile test of a material and the k represents the strain hardening in this bilinear equivalent stress-strain curve. The magnitudes of these parameters are taken from Sturm et al. (2007).

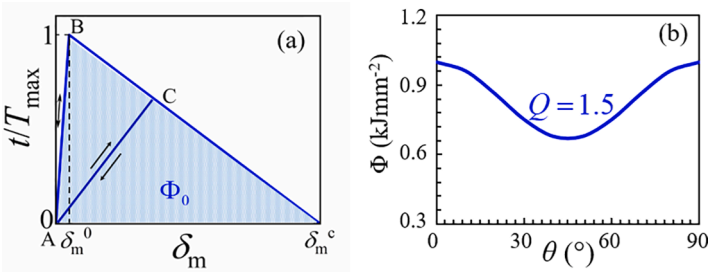

Fig. 8. (a) bi-linear traction-separation relation for the cohesive crack faces, (b) variation of the cohesive energy with grain boundary misorientation angle.

2.3.3. Interfacial traction-separation laws

In order to model arbitrary crack propagation through the grains and GBs, 2D cohesive elements are inserted everywhere within the microstructure region (within the grains and along the grain boundaries). A uniform cross-triangular mesh is used. The cohesive elements are in 0°, ±45°, and 90° directions. The sufficiently fine element size allows any arbitrary crack paths to be resolved within the meaning and limitation of the discrete model. The cohesive elements follow a bilinear traction separation law implemented in ABAQUS 2017. In this cohesive model, the traction applied on any cohesive surface (**t**) is work-conjugate to the interfacial separation ($\boldsymbol{\delta}$).The uncoupled traction-separation constitutive relation can be written as

$$\boldsymbol{t} = \begin{Bmatrix} t_n \\ t_s \end{Bmatrix} = (1-D)\begin{bmatrix} K_{nn} & 0 \\ 0 & K_{ss} \end{bmatrix}\begin{Bmatrix} \delta_n \\ \delta_s \end{Bmatrix}, \tag{19}$$

where $t_n = \boldsymbol{n}\cdot\boldsymbol{t}$, $t_s = \boldsymbol{s}\cdot\boldsymbol{t}$, $\delta_n = \boldsymbol{n}\cdot\boldsymbol{\delta}$, and $\delta_s = \boldsymbol{s}\cdot\boldsymbol{\delta}$ are the normal and shear components of $\boldsymbol{t}$ and $\boldsymbol{\delta}$, respectively, and $\boldsymbol{n}$, $\boldsymbol{s}$ are the unit vectors normal and tangential to the cohesive surface. **K** represents the stiffness tensor connecting $\boldsymbol{t}$ and $\boldsymbol{\delta}$ before damage sets in. K_{nn} and K_{ss} are assumed to be the same. D represents a scalar damage variable. $D = 0$ initially until damage initiates. Damage sets in when the following criterion is satisfied.

$$\left\{\left(\frac{t_n}{t_n^{\max}}\right)^2 + \left(\frac{t_s}{t_s^{\max}}\right)^2\right\} = 1. \tag{20}$$

In our calculations, the maximum cohesive strength is assumed to be the same in both the normal and tangential direction and is denoted as $T_{\max}$.

$$t_n^{\max} = t_s^{\max} = T_{\max}. \tag{21}$$

Since the normal and tangential strengths are taken to be the same and denoted as $T_{\max}$ partly owing to the lack of detailed experimental data for this or similar materials. Future efforts should include experimental measurement of the cohesive parameters using techniques such as in-situ mechanical Raman spectroscopy (MRS) used for composites (Prakash et al., 2018), electronic speckle-pattern interferometry (ESPI) coupled with field projection used for polymers, composites, and elastic crystals (Hong and Kim, 2003; Choi† and Kim, 2007; Chew et al., 2009; Hong et al., 2009); or *J*-integral based methods used for epoxy composites and ductile materials (Chen et al., 2003; Sørensen and Jacobsen, 2003; Fuchs and Major, 2011). The damage initiation criterion can simply be written as,

$$\frac{t}{T_{\max}} = \left\{\frac{t_n^2 + t_s^2}{T_{\max}^2}\right\}^{1/2} = 1. \tag{22}$$

In the above relation, t is the effective traction. When the effective separation ($\delta_m = \sqrt{\delta_n^2 + \delta_s^2}$) reaches a value of δ_m^0, damage initiates, as shown in Fig. 8(a). Before damage initiates, the separation is completely reversible, i.e., upon unloading and reloading, traction follows the same path AB shown in the figure. As a result, no energy is dissipated and $D = 0$. Beyond point B where $\delta = \delta_m^0$, the interfacial strength and stiffness begin to degrade and, upon unloading, the traction follows the path CA, dissipation occurs, and D is calculated as,

$$D = \frac{\delta_m^c\left(\delta_m^{\max} - \delta_m^0\right)}{\delta_m^{\max}\left(\delta_m^c - \delta_m^0\right)}. \tag{23}$$

In the above relation, $\delta_m^{\max}$ represents the hitherto maximum value of the effective separation attained during the loading history up to the current time (i.e., unloading does not affect this value), δ_m^c is the separation for complete failure of the interface. This treatment allows successive unloading and reloading with progressively weakening interfacial strength and stiffness represented by evolving point C and line CA to be tracked and implemented. Upon reloading, the traction follows path AC with the stiffness reduced by the factor of (1-*D*) relative to that embodied in line AB. The interfacial strength and stiffness vanish upon full separation when the effective separation reaches $\delta_m = \delta_m^c$, with $D = 1$ and dissipation reaching the work of separation Φ_0. The limiting value of $D = 1$ corresponds to

Table 3
Cohesive parameters.

Q	K_{nn} (MPa)	$(\Phi_0)_{\max}$(kJ/mm^2)	T_G(MPa)	$T_{GB}^{\min}$(MPa)
1.5	500×10^6	1	962.5	641.67

complete separation.

For the GBs, the cohesive parameters are functions of the misorientation angle, i.e.,

$$\left.\begin{aligned} \Phi_0 &= \Phi_0\left(T_{\max}, \delta_m^c\right), \\ T_{\max} &= \widehat{T}_{\max}(\theta). \end{aligned}\right\} \tag{24}$$

The experimental data for the interfacial strength Watanabe (2011) can be approximated by a sinusoidal function of the form

$$\left.\begin{aligned} T_{GB}(\theta) &= C_1 + C_2\cos(4\theta), \\ C_1 &= \frac{1}{2}\left(T_G + T_{GB}^{\min}\right), \\ C_2 &= \frac{1}{2}\left(T_G - T_{GB}^{\min}\right). \end{aligned}\right\} \tag{25}$$

In the above relations, $T_{GB}(\theta)$ is the misorientation angle dependent $T_{\max}$ as in Eq. (24) with the subscript "max" omitted for brevity and to avoid confusion. $T_{GB}^{\max}$ and $T_{GB}^{\min}$ represent the maximum and minimum values of T_{GB}, respectively. The maximum value $T_{GB}^{\max}$ is taken as the cohesive strength of the grains ($T_{GB}^{\max} = T_G$). Within a grain, the misorientation between two adjacent element sides is zero and hence the cohesive strength remains constant at T_G. Fig. 8(b) shows profile of T_{GB} as a function of the misorientation angle. This profile can be characterized by the ratio $Q = T_G/T_{GB}^{\min}$, which represents the degree of variation of $T_{GB}(\theta)$ as the GB misorientation angle changes. The values of the cohesive parameters are calibrated to match the fracture behavior of Mo as reported in Roy and Zhou (2020). The maximum cohesive energy used in this model scales with the fracture toughness of pure Mo. The range of misorientation-dependent variation of T_{GB} is obtained from experimental data Watanabe (2011). The calibration of the cohesive parameters was described in our previous work Roy and Zhou (2020) and the parameters are given in Table 3. Following the convergence criterion described in Tomar et al. (2004), the lower bound of the cohesive finite element size is estimated as

$$d_z \geq \frac{\lambda_o \delta_{sc}}{T_{\max}} \frac{\overline{E}}{(1-\overline{\nu}^2)} \frac{\sqrt{2}+1}{1-\overline{\nu}} = 0.006\ \mu\text{m}, \tag{26}$$

whereas, the upper bound is

$$d_z \leq \frac{9\pi}{32} \frac{\overline{E}}{(1-\overline{\nu}^2)} \frac{\Phi_0}{T_{\max}^2} = 360\ \mu\text{m}. \tag{27}$$

A cross-triangular mesh with linear plane strain CPE3 elements are used to model the bulk grains. The COH2D4 type cohesive element of size 5 μm used in this work falls well within this range and also sufficiently resolves the grain structure.

2.4. Evaluation of fracture toughness and fracture micromechanisms

We calculate K_{IC} via the J-integral (Rice, 1968) is defined by

$$\left.\begin{aligned} J &= \int_\Gamma \left(w dy - \boldsymbol{T} \cdot \frac{\partial \boldsymbol{u}}{\partial x} ds \right), \\ w &= \int_0^{E_{ij}} \boldsymbol{\tau} : d\mathbf{E}, \\ E_{ij} &= \frac{1}{2}\left(F_{ki}F_{kj} - \delta_{ij}\right). \end{aligned}\right\} \tag{28}$$

In the above relations, $\boldsymbol{T}$ is the traction vector on a surface with normal $\boldsymbol{n}$ in the reference configuration, $\boldsymbol{u}$ is the displacement, $\boldsymbol{\tau}$ is the Kirchhoff stress, E_{ij} are components of the Lagrangian strain $\mathbf{E}$ which is work-conjugate to $\boldsymbol{\tau}$ in the reference configuration, and F_{ij} are the components of the deformation gradient $\mathbf{F}$. Γ is the crack tip contour along which the integral is calculated, as indicated in Fig. 1. The J value at crack initiation is denoted as J_i and the value corresponding to the attainment of steady-state is termed as J_{ss}. For J_{IC} calculations to be valid,

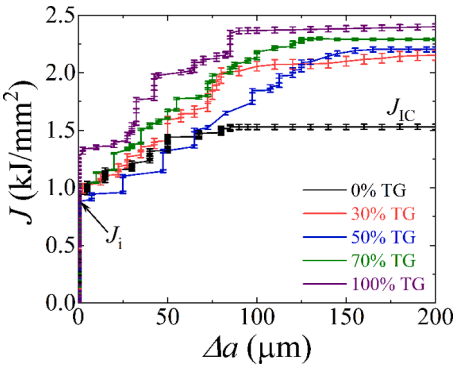

Fig. 9. The crack growth resistance curves for five proportions of textured grains in the microstructure.

$$a, (W-a), b \geq \frac{25 J_{ss}}{\sigma_y}. \tag{29}$$

The specimen configuration satisfies this condition. The J-integral accounts for energy dissipated through both surface creation and plasticity around the crack tip. Thus, the J-integral can be decomposed into a surface contribution and an inelastic contribution, i.e.,

$$J = J_S + J_P. \tag{30}$$

The surface part J_S can be easily evaluated and has the dependence in the form of

$$J_S = \Phi_0\left(T_{\max}(\theta), \delta_m^c\right). \tag{31}$$

Eqs. (30) and (31) allow the plastic dissipation rate $J_P$to be calculated readily. It is used to quantify the contribution of plasticity to fracture resistance.

Once J_{IC} is calculated under small scale yield conditions, K_{IC} is obtained via

$$K_{IC} = \sqrt{\frac{J_{IC}\overline{E}}{1-\overline{\nu}^2}}. \tag{32}$$

The CFEM based model explicitly tracks the intergranular and transgranular fracture mechanisms. The fractions of the crack path associated with transgranular fracture and intergranular are given by

$$\left.\begin{aligned} H_g &= \frac{L_g}{L_g + L_{gb}}, \\ H_{gb} &= \frac{L_{gb}}{L_g + L_{gb}}. \end{aligned}\right\} \tag{33}$$

L_g and L_{gb} represent the lengths of crack in each type of fracture sites. The $L = L_g + L_{gb}$ is total crack length. The crack path tortuosity (ξ) is

$$\xi = \frac{L}{a}, \tag{34}$$

where a is the projected crack length in the overall direction of propagation. J_S can be expressed in terms of the crack path descriptors as

$$J_S\left(H_g, H_{gb}, \xi, \Phi_0\right) = \xi\left(H_g\Phi_g + H_{gb}\Phi_{gb}(\theta)\right). \tag{35}$$

In the above relation, Φ_g and Φ_{gb} are, respectively, the work of separation for the grains and the GBs. The multiple instantiations of statistically similar microstructures are used to account for the stochasticity in fracture behavior and fracture toughness.

3. Results

The results of the microstructure-based CFEM calculations, the subsequent fracture toughness characterization, and analyses are discussed in this section. All samples in the statistically equivalent microstructure sample sets are subjected to the same loading conditions. Systematic comparisons of the fracture trends and the mechanisms are made in terms of K_{IC}, J_{IC}, H_g, H_{gb} and ξ.

To delineate the effect of grain orientation (texture), five sets of simulations are performed using the five statistically equivalent microstructure sample sets with different fractions of TG embodied in Fig. 3. Fig. 9 shows the crack growth resistance curves for the five statistically equivalent microstructure sample sets. Both the average and the range of variations among the five samples in each set are shown. The J value at crack initiation (J_i) is taken as the fracture initiation resistance. The initiation resistance is significantly

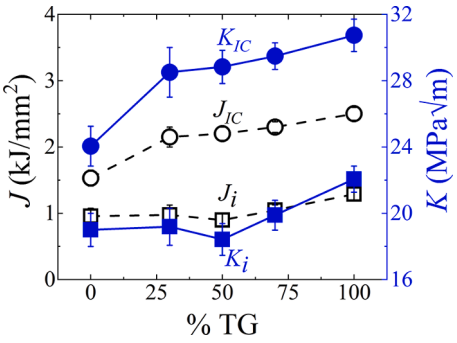

Fig. 10. Fracture resistance in terms of J_i, J_{IC}, K_i, and K_{IC} as a function of the proportion of textured grains in the microstructure.

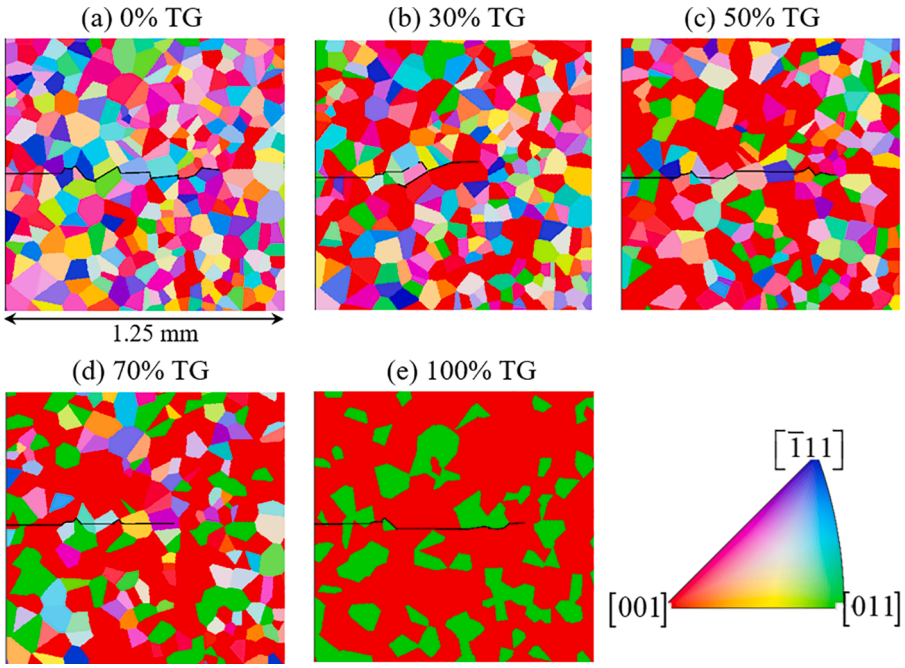

Fig. 11. Crack propagation in representative microstructures from the five SEMSS.

higher for the 100% TG case compared to all other cases which have similar values. The fracture resistance when crack growth attains a steady state is defined as the steady state fracture toughness J_{IC}. The J_{IC} increases as the level of texture increases.

Fig. 10 shows the initiation and steady state fracture resistance in terms of J_i, K_i, J_{IC}, and K_{IC} as functions of the fraction of TG. The error bars denote statistical variations among the five samples in the statistically equivalent microstructure sample sets. The initiation toughness does not vary significantly as the fraction of TG increases, however, K_i is considerably higher for the mcrostructures with 100% TG. On the other hand, there is an overall increase in K_{IC} as the fraction of TG increases. Fig. 11 shows the crack propagation path in a representative microstructure from each of the five statistically equivalent microstructure sample sets. In the microstructure sample set with 0% TG, crack propagation is almost entirely intergranular, through GBs. In the microstructure sample set with 30% TG, partial transition from intergranular to transgranular crack growth occurs as the crack encounters longer mean free path for fracture through the grains of the {011}<100> texture. As the fraction of TG further increases (50 –70%), transgranular fracture dominates as the crack cuts through the grains of both random orientations and the {011}<100> texture. At 100% TG, fracture is entirely through grains of the {011}<100> texture and boundaries between {011}<100> and {001}<110> oriented grains, with no propagation through {001}<110> orientated grains. Overall, the extent of transgranular fracture increases as the fraction of TG increases. The interplays between the fracture mechanisms are quantified in terms of the fractions of crack path in each type of site (H_g and H_{gb}) as defined in Eq. (33) and crack tortuosity ξ as defined in Eq. (34), the result is shown in Fig. 12. The fraction of intergranular crack path (H_{gb}) and crack path tortuosity ξ both decrease as the fraction of TG increases, as transgranular fracture (cleavage) is primarily straight in directions aligned favorably for crack growth. This observation is consistent with the trend shown by the overall fracture toughness values in Fig. 10. Fig. 13 delineates the competition between plastic deformation and crack face generation in terms of their relative

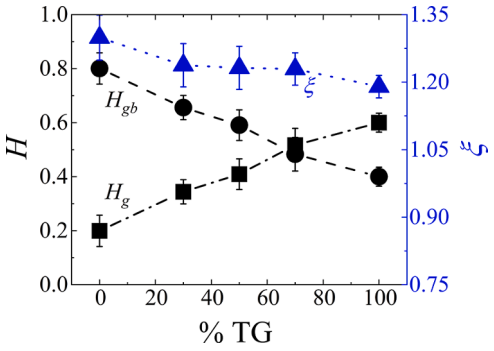

Fig. 12. Fractions of crack lengths inside grains (H_g) and along grain boundaries (H_{gb}) and the crack path tortuosity (ξ) at different levels of texture.

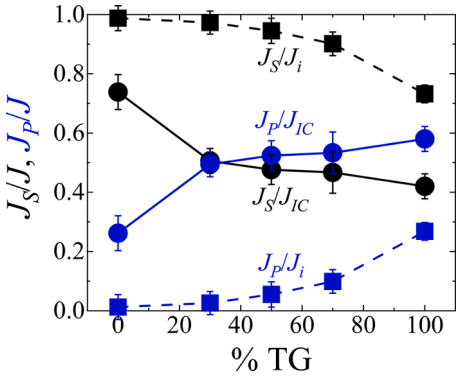

Fig. 13. Relative contributions of plastic dissipation and surface energy release to the initiation and steady state fracture resistance at different levels of texture.

contributions to the overall fracture resistance. The relative contribution of new surface creation to the overall energy release rate decreases and the relative contribution of plasticity increases as the level of texture increases, as expected. The same trend holds both for crack initiation and steady state crack propagation.

To validate the computational model, the result for 0% TG is compared with the experimental observations reported in Sturm et al. (2007). Specifically, the experimentally measured K_{IC} for unalloyed Mo with a grain size of ~97 μm is 21.9–26.5 MPa$\sqrt{\text{m}}$. The computationally predicted K_{IC} is 24.04 ± 1.2 MPa$\sqrt{\text{m}}$. In the experiments, fractographic analysis of the fracture surfaces reveals a dominance of intergranular fracture with only a few instances of transgranular fracture. The computational model echoes this in showing that intergranular crack propagation is the dominant mechanism at 0% TG. The model is in good agreement with experiments in terms of both fracture toughness and micromechanisms.

4. Discussion

Texture influences microstructure in multiple ways. Variation in the fraction of TG leads to variation in (1) the effective grain size distribution, (2) the fraction of grains with favorably oriented PSS, and (3) GB characteristics. To understand the overall effect of texture on fracture in terms of fracture toughness, the competition between fracture mechanisms, and the competition between plasticity and crack face creation, the effects of the three aspects are discussed.

4.1. *Effect of grain size*

The grain size determines the mean free path for transgranular fracture and thus influences primarily the plasticity part of the overall fracture resistance as is evident from our prior work (Roy and Zhou, 2020). As the fraction of TG increases, the maximum effective grain size increases although the mean grain size remains nearly the same. At 0% TG, the grain size is evenly distributed around the mean of ~70 μm. At 50–70% texture, randomly distributed islands of grains with the ~70 μm mean intercept grain size are embedded in a relatively coarse matrix of TG. The mean intercept grain size of the coarser grains increases as the fraction of TG increases. Fig. 14 shows that K_{IC} is higher at higher values of the maximum grain size. This is attributed to the higher contribution of plastic dissipation associated with transgranular crack seen in this figure. This is in agreement with the observations reported by Molkeri et al. (2019) and the computational results reported by Roy and Zhou (2020).

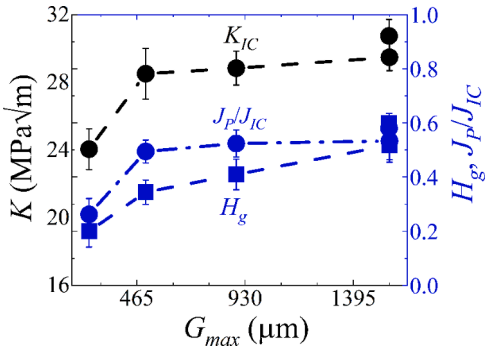

Fig. 14. Fracture toughness in terms of K_{IC}, relative contribution of plasticity to J_{IC}, and the transgranular crack path ratio at different levels of maximum grain size.

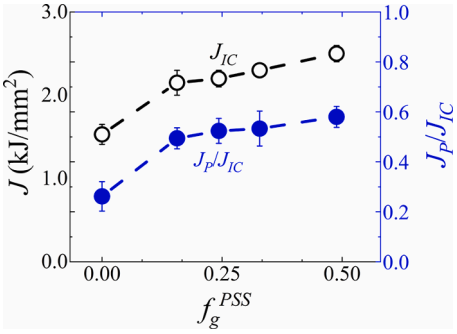

Fig. 15. Fracture resistance in terms of J_{IC} and relative contribution of plasticity to J_{IC} as functions of the fraction of grains with favorably oriented primary slip system (PSS).

4.2. *Effect of favorably oriented PSS*

As reported in the literature (e.g., Gröger and Vitek (2009)), the critical resolved shear stress for slip is the lowest for the $(\bar{1}01)[111]$ slip system, followed by $(0\bar{1}\bar{1})[11\bar{1}]$, $(0\bar{1}1)[\bar{1}11]$, and $(101)[\bar{1}\bar{1}1]$, in that order. Due to the single slip assumption, only one slip system can be activated in each grain. Even low levels (<0.25%) of plastic strain at the crack tip can significantly impede fracture initiation. As the fraction of grains with a PSS of lower critical resolved shear stress aligned with the specimen plane increases, enhanced plasticity leads to higher fracture resistance. In the current analysis, grains with the $(\bar{1}01)[111]$slip system within the Goss texture component have a CRSS that is lower than that of the $(0\bar{1}1)[\bar{1}11]$ slip system within the rotated cubic texture component (Fig. 11(e)). As texture increases, the fraction of grains with favorably oriented PSS in the Goss component increases, resulting in the microstructures showing a contiguous matrix of such grains at the higher TG fractions of 70% and 100%. This matrix with grains of similarly oriented grains behave somewhat like a single crystal. This trend is key to explaining the trend in Fig. 15. As texture increases, crack tends to propagate through the single-crystal-like matrix with the Goss texture component, mostly bypassing the isolated islands of grains with the rotated cubic texture component. Since the transgranular crack propagation through the matrix of similarly oriented grains with the Goss texture results in significant plastic dissipation around the growing crack tip, the relative contribution of plasticity to steady state fracture resistance increases as the level of texture increases, leading to the overall higher fracture resistance as shown in the Fig. 15. Here, the assumption of single slip contributes to this outcome. A 3D model or 2D models allowing multiple planar slips can better enable the interplay between fracture and slip systems. The simplified model here is a first step and does a reasonable job in capturing the trends in fracture involving primary slip.

4.3. *Effect of GB characteristics*

Note that for simplicity, GBs are characterized based on only their misorientation angle. No symmetry operation is performed and hence the misorientation angle ranges between 0° and 180°. Previous work (Roy and Zhou, 2020) shows that the overall fracture resistance increases as the density of weaker GB decreases. In this case, the weaker GB density decreases almost linearly as the fraction of TG increases, causing the crack to increasingly propagate in a transgranular manner (Fig. 16). A consequence is the relative contribution of crack face generation to the overall fracture resistance is lower at higher levels of texture. The crack path tortuosity also follows the same trend as the intergranular crack path ratio.

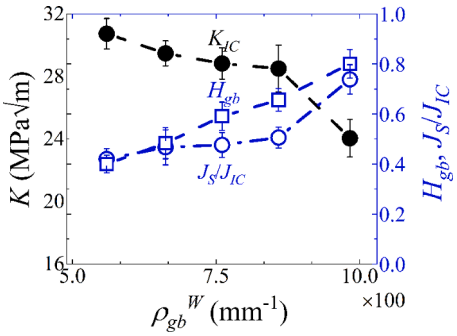

Fig. 16. Fracture toughness in terms of K_{IC}, relative contribution of surface energy to J_{IC}, and the intergranular crack path ratio for different levels of weaker GB density.

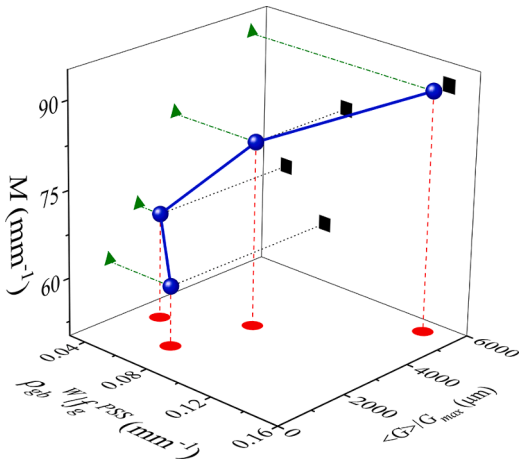

Fig. 17. The microstructure descriptor (M) as a function of the grain size distribution descriptor and the ratio of weaker GB density to the fraction of grains with favorably oriented primary slip systems.

4.4. Correlation between fracture behavior and microstructure attributes

The relations between fracture behavior and microstructure attributes are analyzed with account of statistical uncertainties arising from microstructure heterogeneities. To this effect, the contributions of surface energy and plasticity are assessed as functions of the grain size, fraction of grains with favorably oriented PSS, and misorientation-dependent weaker GB density. To quantify the microstructure attributes, a microstructure descriptor M that takes into account the effective grain size distribution, fraction of PSS, GB strength profile, and the misorientation-dependent weaker GB density is defined in mm^{-1} as,

$$M = (Q-1)\rho_{gb}^{W}\left(\frac{1}{f_g^{PSS}}\right)\sqrt{\frac{\langle G\rangle}{G_{\max}}}, \tag{36}$$

where, ρ_{gb}^{W} is in mm^{-1}. The grain size distribution is characterized by the ratio of the mean intercept grain size ($\langle G\rangle$) to the maximum grain size($G_{\max}$). This ratio signifies the skewness in the grain size distribution. The GB strength profile is quantified by the parameter Q which is the ratio of the maximum GB strength to the minimum GB strength. Parameter Q signifies level of the GB strength relative to the fracture strength of the grains and is kept constant at 1.5 for all calculations. Fig. 17 shows M as a function of the grain size distribution descriptor and the ratio of weaker GB density to the fraction of grains with favorably oriented PSS. The weaker GB density and the fraction of PSS have opposite effects on the overall fracture toughness. $M = 0$ represents a homogeneous material with no microstructural heterogeneities. $M \to \infty$ when the microstructure contains only weaker GBs and no significant fraction of grains with favorably oriented PSS. M is defined in such a way that for each statistically equivalent microstructure sample sets, the intergranular crack path fraction can be expressed as

$$H_{gb} = 1 - \exp\left[-\left(\frac{M}{M_0}\right)^{m}\right], \tag{37}$$

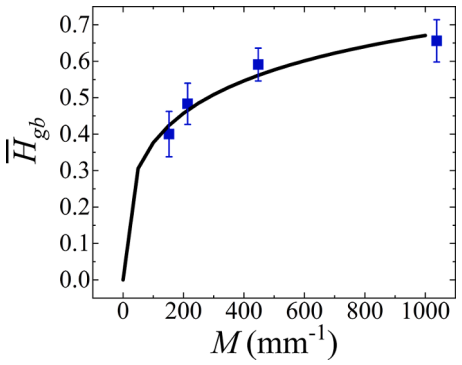

Fig. 18. Mean fraction of intergranular crack path as a function of the microstructure descriptor M.

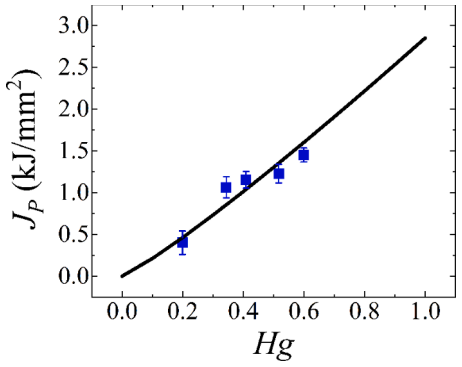

Fig. 19. The contribution of plasticity as a function of the fraction of transgranular crack path.

where M_0 is a reference value in mm^{-1} and m is the exponent. This specific form of M is somewhat informed by our previous work (Roy and Zhou, 2020). This form satisfies the limiting conditions of $H_{gb} \to 1$ as $\rho_{gb}^{W} \to \infty$ (the microstructure contains only weaker GBs and cracks tend to propagate entirely through the GBs, leading to $M \to \infty$) and/or as $f_g^{PSS} \to 0$ (none of the grains in the microstructure has favorably oriented PSS). Note that $H_{gb} = 1$ corresponds to the case of fracture being completely governed by relative surface energy. On the other hand, if $G_{\max} \gg \langle G \rangle$ (the grain size distribution is highly skewed to small size end) and/or $\rho_{gb}^{W} \to 0$ (the material has no microstructural heterogeneities), $M \to 0$ and consequently $H_{gb} \to 0$. Under such a scenario, cracks tend to propagate entirely through the grains. The results from the five statistically equivalent microstructure sample sets are used to obtain the values of M_0 and m. For the material analyzed, $M_0 = 753.47\mathrm{mm}^{-1}$ and $m = 0.3714$. Fig. 18 compares the calculated results from simulations and the fit to Eq. (37).

The surface part of the energy release rate J_S can be evaluated using Eqs. (35) and (37) as a function of the microstructure descriptor. For each material case (each statistically equivalent microstructure sample sets), the mean value of J_S can be expressed as a function of the mean crack path tortuosity ($\overline{\xi}$) and the mean GB energy ($\overline{\Phi}_{gb}$), i.e.,

$$\overline{J}_S = \overline{\xi}\left[\overline{\Phi}_{gb} + \left(\Phi_g - \overline{\Phi}_{gb}\right)\exp\left\{-\left(\frac{M}{M_0}\right)^m\right\}\right], \tag{38}$$

where $\Phi_g, \overline{\Phi}_{gb},$ and $\overline{J}_S$ are in $\mathrm{kJ/mm}^2$. As expected, when $M = 0$, $\overline{J}_S = \overline{\xi}\Phi_g = \overline{J}_S^g$, which is the surface part of the energy release rate for a uniform material without microstructure. On the other hand, when $M \to \infty$, $H_{gb} \to 1$, and $\overline{J}_S \to \overline{\xi}\overline{\Phi}_{gb} \to \overline{J}_S^{gb}$, which is the average surface energy release rate due to GBs only.

To assess the contribution of plastic dissipation, J_P is plotted as a function of the fraction of transgranular path in Fig. 19. The relation can be described by

$$J_P = J_P^g\left(H_g\right)^n = J_P^g\left(1 - H_{gb}\right)^n, \tag{39}$$

where, J_P^g is the plastic dissipation for a homogeneous material without GB and is measured in $\mathrm{kJ/mm}^2$. When $H_g = 1$, the material is homogeneous, $H_{gb} = 0$, and $J_P^g = 2.85\ \mathrm{kJ/mm}^2$ and $n = 1.13$. For each statistically equivalent microstructure sample set, Eqs. (37) and (39) allow the mean value of J_P to be obtained as a function of the microstructure descriptor as

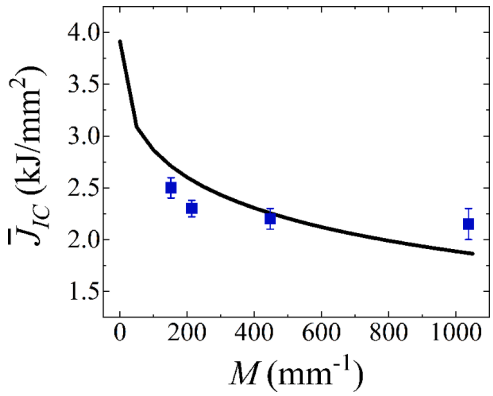

Fig. 20. Mean fracture resistance as a function of the microstructure descriptor. The discrete data points are obtained from simulations and the solid line represents eq. (41).

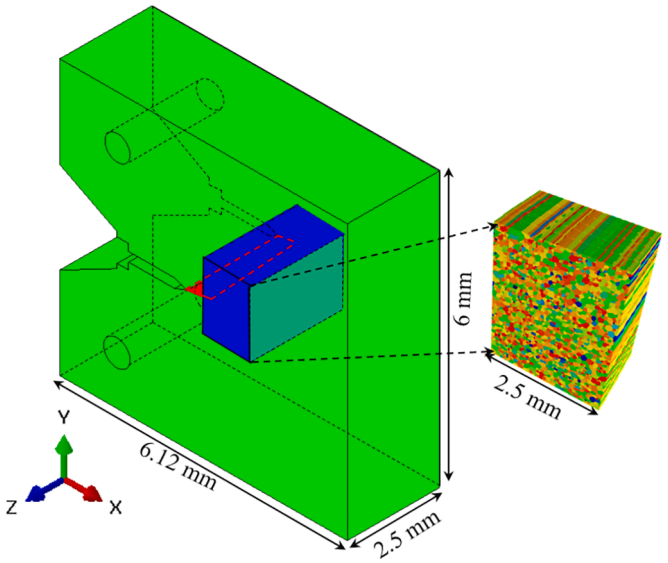

Fig. 21. 2.5D computational model with columnar microstructure.

$$\bar{J}_P = J_P^g \exp\left\{ -\left(\frac{M}{M_0}\right)^{mn} \right\}. \tag{40}$$

Finally, the mean value for J_{IC} can be obtained as a function of the microstructure descriptor by combining Eqs. (38) and (40). The relation is given by

$$\bar{J}_{IC} = \bar{J}_S^{gb} + \left(\bar{J}_S^g - \bar{J}_S^{gb}\right) \exp\left\{ -\left(\frac{M}{M_0}\right)^{m} \right\} + J_P^g \exp\left\{ -\left(\frac{M}{M_0}\right)^{mn} \right\}. \tag{41}$$

Again as expected, when $M = 0$, $\bar{J}_{IC} = \bar{J}_S^g + J_P^g$; and when $M \to \infty$, $\bar{J}_{IC} \to \bar{J}_S^{gb}$, the contribution from plasticity becomes negligible. Fig. 20 compares the semi-empirical model with the computationally obtained results. The trend and values are in reasonably good overall agreement. The data points and the relation allow the mean fracture resistance to be expressed as a function of microstructure attributes. It is hoped that experimental data can be obtained in the future to provide verification of this relation which can then potentially be used in microstructure design.

4.5. Extension of framework to 2.5D and comparison with 2D

The trends described above are obtained from 2D plane strain simulations using statistically similar microstructure sets under the single slip assumption. In order to understand how the trends change when aspects of the 3D nature of the microstructures are considered, a two-and-a half dimensional (2.5D) model with columnar microstructures under generalized plane strain conditions is

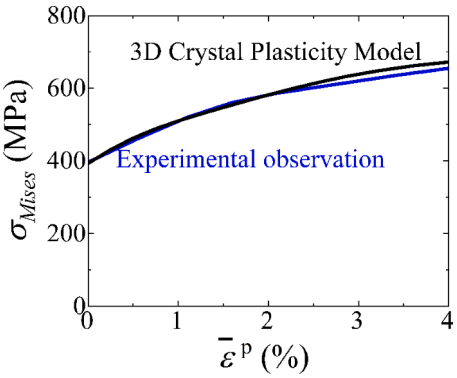

Fig. 22. Comparison of the Mises effective stress – strain response calculated from the 3D crystal plasticity model with experimental observation as reported in Sturm et al. (2007).

Table 4
Parameters of the 3D crystal plasticity model.

$\dot{\gamma}_0$ (s^{-1})	m	A_{kin} (MPa)	A_{dyn}	H	$q^{\alpha\beta}$ (MPa)	a_1	a_2	a_3
0.1	13	8	4000	485	1.4	0.24	0.35	0

developed. This 2.5D model is a fully 3D model implemented in a simplified manner to allow aspects of the out-of-plane deformation mode (including both out-of-plane strain and activation of out-of-plane slip systems) to be considered under the generalized plane strain condition. Specifically, the 2.5D model uses one row of 3D elements in the out-of-plane direction (Z-axis in Fig. 21) to describe columnar grains. The surfaces of the specimen are constrained such that the displacement field in the material has the form

$$u = u(X, Y), v = v(X, Y), \text{ and } w = kZ, \tag{42}$$

where, k is a constant which represents the average normal strain (to the first order approximation) in the specimen. The linear dependence on Z (achieved via proper choice of finite element type and implementation of boundary condition as discussed below) ensures that the strains are constant in the Z direction and strain component E_{zz} in the thickness direction is non-zero in addition to the in-plane strain components E_{xx}, E_{yy}, and E_{xy}. This is in contrast to a strict plane strain model for which

$$u = u(X, Y), v = v(X, Y), \text{ and } w = 0; \tag{43}$$

and the only non-zero strain components are E_{xx}, E_{yy}, E_{xy}.

Linear triangular CPEG3 type elements in ABAQUS are used to implement this generalized plane strain formulation. The CPEG3 elements are constant-strain elements that ensure that each of the two surfaces of the specimen $(Z = 0 \text{and} Z = 2.5 \text{mminFig.21})$ moves as a rigid plane, thereby allowing the conditions of the 2.5D model stated above to be implemented. In particular, the CPEG3 elements use the 3-node geometry of classical plane strain CPE3 linear triangular elements to model the two bounding planes and allow one being an image of the other. As shown in Fig. 21, the model captures the 3D CT specimen geometry with a specified thickness ($t = 2.5$ mm) in the Z-direction. Just like in the 2D model, mode-I loading is imposed by specifying load-point displacements shown in Fig. 1. Load-point displacements are specified with the general multiple point constraint (MPC) on the surface of the hole. A constant longitudinal strain in the Z direction $(E_{zz} = 0.001)$ is specified by assigning 0.1% reduction in the thickness of the specimen.

A fully 3D crystal plasticity model that admits all 24 bcc slip systems is adopted in the microstructure region. In contrast to the 2D plane strain model, slip is now allowed in the out-of-plane direction as long as the strain compatibility conditions are satisfied. Multiple slips can be activated in the 2.5D model, depending on the CRSS. Cross-slip is allowed. As a result, the overall plastic dissipation around the crack-tip can be higher. To calibrate the parameters for this model, a full 3D simulation of the uniaxial tensile test is carried out. The stress-strain curve obtained closely matches the experimentally measured stress-strain relation (Fig. 22). The parameters are given in Table 4. To capture crack propagation in the 2.5D model, a 3D misorientation-dependent cohesive traction-separation law (Appendix B) is adopted. The quasi-static boundary value problem is solved in ABAQUS/Standard in conjunction with an UMAT for the 3D crystal plasticity formulation.

The microstructure sample sets used in this 2.5D model are the same as those used in the 2D model as shown in Fig. 3. The only difference is that in this 2.5D model slip is allowed in the out-of-plane Z direction. The crack propagation paths obtained from the 2D and 2.5D models are generally quite similar, as shown in Fig. 23 using the cases of 0%, 50%, and 100% texture. Indeed, the corresponding crack path descriptors calculated from the two models follow nearly the same trend (not shown). The fracture resistance measures of J_i, J_{IC}, K_i, and K_{IC} are compared in Fig. 24. The same general trend is seen in the results from both models, with the 2.5D model showing consistently higher fracture resistances. Fig. 25 compares the corresponding crack growth resistance curves. In all the cases, the 2D model underestimates the steady-state fracture resistance relative to the 2.5D model. This is attributed to the fact that the

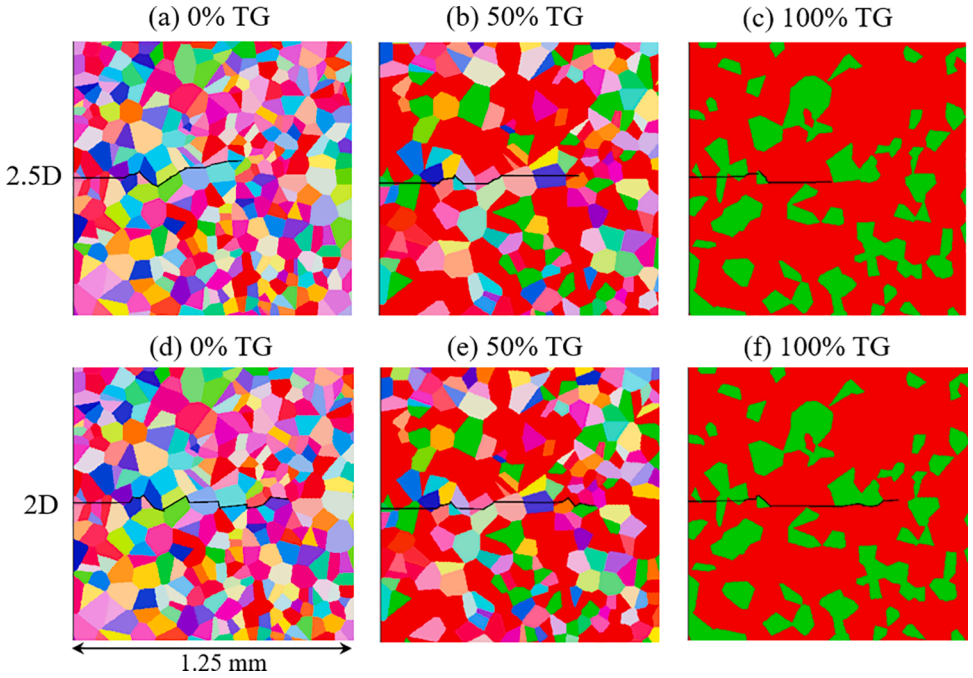

Fig. 23. Comparison of the crack paths obtained from 2.5D and 2D models.

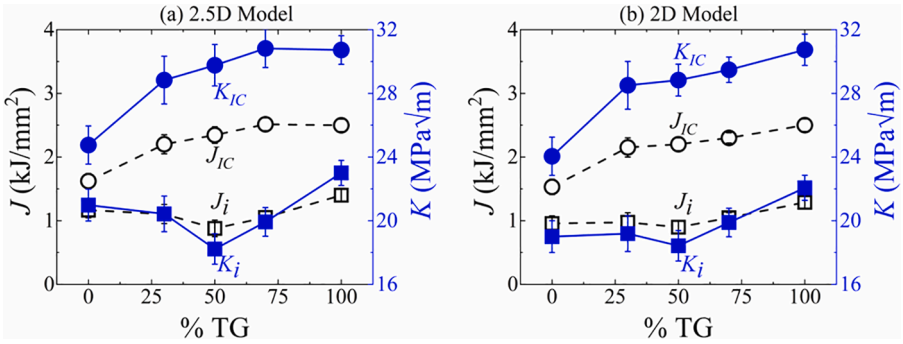

Fig. 24. Fracture toughness measures as a function of texture predicted by (a) 2.5D model (b) 2D model.

fully 3D crystal plasticity formulation in the 2.5D model allows for greater levels of plasticity and the dissipation associated with it through the activation of multiple slip systems. The enhanced plasticity occurs not only in the interior of the grains but also near the GBs. In case of the microstructure with 100% TG, transgranular fracture dominates and the material acts in a manner similar to that of a single crystal (Fig. 3(e)). Under such a scenario, the primary slip system is the only favorably orientated system even in the 2.5D model, resulting the results to be the same for both models.

To account the effect of the enhanced plastic dissipation in the 2.5D model, Eq. (41) is modified to

$$\overline{J}_{IC} = \overline{J}_S^{gb} + \left(\overline{J}_S^{s} - \overline{J}_S^{gb}\right)\exp\left\{-\left(\frac{M}{M_0}\right)^{m}\right\} + J_P^{s}\exp\left\{-\left(\frac{M}{M_0}\right)^{mn}\right\} + J_P^{gb}\left[1-\exp\left\{-\left(\frac{M}{M_0}\right)^{m}\right\}\right]^{q}. \tag{44}$$

Here, J_P^{gb} represents the enhanced plastic dissipation at GBs. To accurately describe the results, all the parameters above must be determined using data from the 2.5D model. Such an analysis, including the determination of the specific form of J_P^{gb} is not undertaken here and can be the focus of a future study.

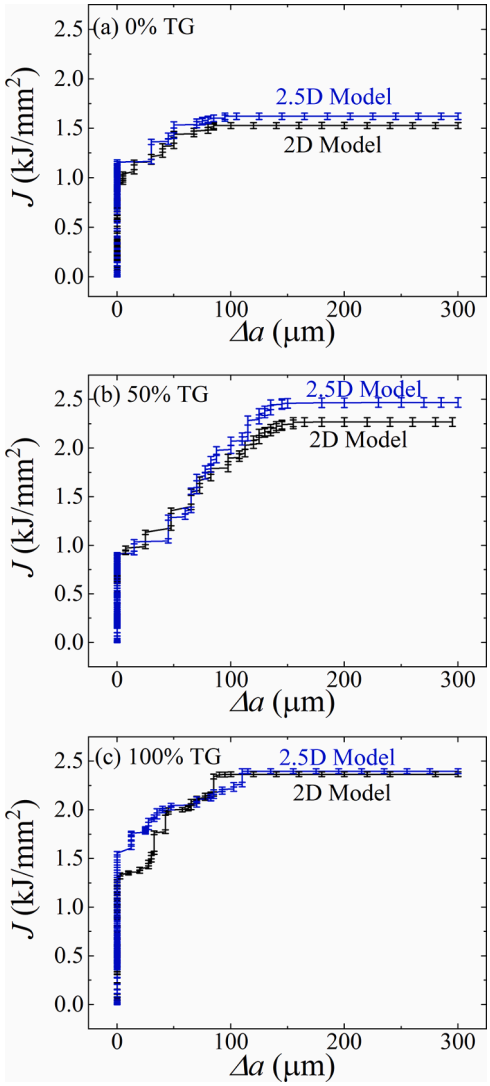

Fig. 25. Comparison of the crack growth resistance curves obtained from 2.5D and 2D models for microstructures with (a) 0%, (b) 50%, and (c) 100% textured grains.

5. Summary and conclusions

In this paper, a framework for capturing the interplay between GB structure and constituent plasticity in ductile metals during fracture is developed. This framework allows the effects of grain orientation and texture on deformation, crack initiation/propagation, and fracture resistance to be analyzed and quantified. This framework is used to explore the fracture behavior of bcc-structured polycrystalline Mo, with the fracture toughness of the material predicted as a function of microstructure attributes. The focus of the analysis carried out is on the effects of grain orientation/texture, grain size, and misorientation-dependent GB characteristics.

The prediction of the fracture resistance measures J_{IC} and K_{IC} uses a J-integral based method which captures the competition between transgranular and intergranular fracture and the tradeoff between microstructure-induced crack tortuosity and constituent plasticity. Computations are carried out primarily in 2D and the differences between 2D and 2.5D are outlined. The results show that the overall fracture toughness increases as the texture increases, pointing out the benefit of strategically skewing the microstructure and taking advantage of the microstructure anisotropy. The results also suggest, for the setting analyzed, the benefits of changing the effective grain size distribution to increase the mean free path for transgranular crack propagation, favorably oriented primary slip systems. The underlying mechanisms for these measures are enhancement of plastic dissipation, proper balance between transgranular/intergranular crack propagation, and balance between plasticity and crack tortuosity.

Empirical relations are developed to relate the fracture toughness of the material to the effective grain size distribution, fraction of

favorably oriented slip systems, weaker GB density, and GB strength. The overall predicted fracture toughness levels are in general agreement with data reported in the literature, as stated earlier.

Overall, the framework should be considered a first step effort, as the model includes significant simplifications and idealizations, including the single-slip assumption, 2D or 2.5D plane strain nature of the models, and consideration of the only two primary texture components of the material. Although the same sets of microstructures are used in both 2D and 2.5D models, activation of out-of-plane deformation modes in the 2.5D model results in enhanced plastic dissipation around the crack. However, the general trend between fracture toughness and texture remains the same. This establishes the applicability of the overall trends obtained from the 2D and 2.5D models to 3D situations with certain caveats. Note that the analysis carried out involves only two specific orientations of the texture components relative to the macroscopic specimen geometry. Future work should include extension of the framework to full 3D, account for more random orientations of textured microstructures relative to the specimen geometry, and experimental validation, leading to more detailed understanding of the relations between microstructure and macroscopic fracture resistance and tools for designing fracture-resistant materials.

Declaration of Competing Interest

None.

Acknowledgment

UR gratefully acknowledges valuable discussions with Krzysztof S. Stopka and Theodore Zirkle during the developmental stage of the crystal plasticity model.

CRediT author statement

Ushasi Roy: Conceptualization, methodology, software, validation, formal analysis, investigation, writing-original draft.
David L. McDowell: Conceptualization, methodology, writing - review and editing.
Min Zhou: Conceptualization, writing – review and editing, supervision, project administration.

Appendix A. Effect of orientation distribution on fracture toughness

To study the effect of crystallographic texture on fracture, computationally generated microstructures with systematically varying crystallographic texture are designed and used. The two basic texture components for cubic materials are considered: (1) the Goss texture with {110}<001> preferred orientation and (2) the brass texture with the {011}<211> preferred orientation. A statistically similar microstructure sample set generated by Voronoi tessellation (Fig. 2) is used. Two sets of microstructures are generated, each set with a distinct texture component conforming to one of two specific orientation distribution function (ODF) profiles centered around {110}<001> or {011}<211>. The open source software suite DREAM.3D is used to create the orientation maps for each statistically similar microstructure sample set (SEMSS). The orientation distribution generator uses 3 parameters to formulate the specific orientation distribution profile: (1) the set of Euler angles describing crystallographic orientation, (2) a weight parameter for the orientation, and (3) a parameter σ_{ODF} that represents the spread to allow deviations of individual grains around the preferred orientation. Two sets of Euler angles (0°, 45°, 0°) and (35°, 45°, 0°) are used to represent the Goss and brass texture, respectively. A weight value of 500,000 is used to generate a strong texture following the conventional norm. Four values of σ_{ODF} 1, 3, 5, and 7 are used to generate systematic variations in the crystallographic texture maps. Within each set with a distinct texture component (brass or Goss), the extent of texture is varied in four levels by gradually increasing the spread σ_{ODF} from the preferred orientation of the corresponding ODF as shown in Fig. A1. Thus, a total of $4 \times 2 = 8$ statistically equivalent microstructure sample sets are generated, each containing five microstructural instantiations which are statistically similar in terms of grain size distribution and orientation distribution. Fig. A1 shows one representative instantiation from each of the 8 statistically equivalent microstructure sample sets with the corresponding (011) pole figures indicating the orientation distribution functions. These microstructures are used in the 2D model. The 2D crystal plasticity formulation is adopted for the grains. Misorientation-dependent 2D traction-separation laws are assumed for the interfaces. Finally, *J*-integral values are determined along the contour shown in Fig. 1 as a function of crack extension to obtain the initiation and steady-state fracture resistance values. Fig. A2 shows the thus obtained J_i, J_{IC}, K_i, K_{IC} values as functions of the ODF descriptor σ_{ODF}. The dependence of the initiation or steady-state fracture toughness on the systematically varying crystallographic texture distributions seems to be negligibly small. This can be attributed to the fact that although the density of a particular preferred orientation changes from one statistically equivalent microstructure sample set to another, the grain orientations lie closely to the target orientation, resulting in a lower density of high angle GBs. High angle GBs usually affect the otherwise continuous crack paths and influence the overall fracture toughness values.

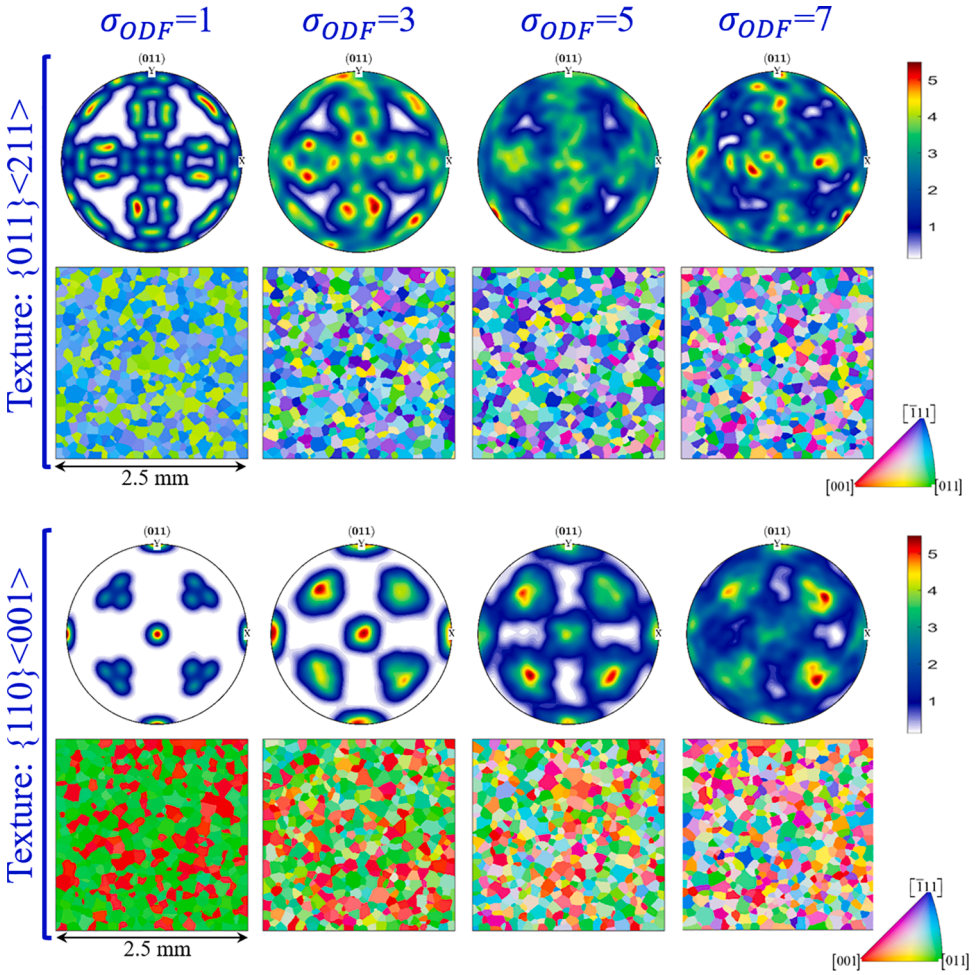

Fig. A1. One out of the five instantiations of microstructure and the corresponding (011) pole figure from each of the eight statistically equivalent microstructure sample sets (SEMSS). The σ_{ODF} increases from left to right. The colors in the stereographic triangle indicate the crystalline plane normals of grains parallel to the XY plane normal of the specimen in Fig. 1.

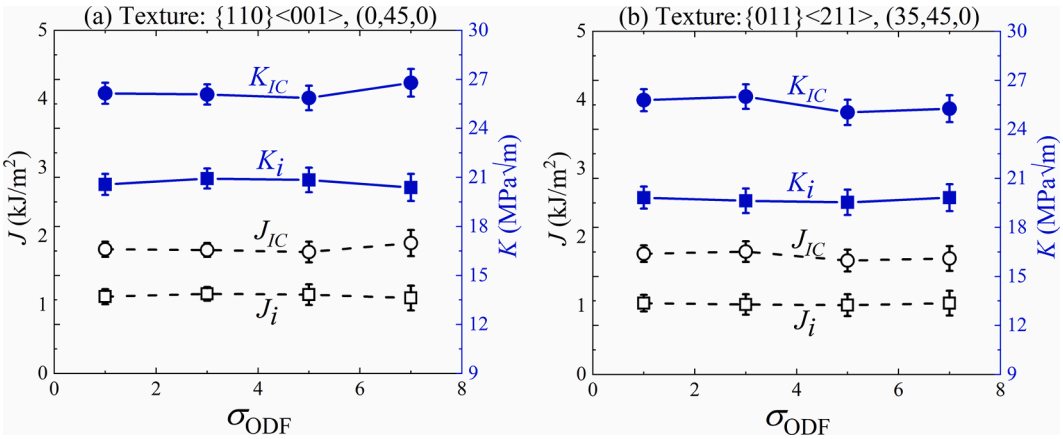

Fig. A2. Dependence of fracture toughness measures on the ODF descriptor (σ_{ODF}) representing the deviation from a particular texture component, (a) the {110}<001> texture and (b) the {011}<211> texture.

Appendix B. 3D interfacial traction separation law

The traction-separation constitutive relation in 3D used in the 2.5D model is

$$\boldsymbol{t} = \begin{Bmatrix} t_n \\ t_s \\ t_t \end{Bmatrix} = (1-D)\begin{bmatrix} K_{nn} & 0 & 0 \\ 0 & K_{ss} & 0 \\ 0 & 0 & K_{tt} \end{bmatrix} \begin{Bmatrix} \delta_n \\ \delta_s \\ \delta_t \end{Bmatrix}, \tag{B.1}$$

where $\boldsymbol{t}$ represents the nominal traction vector which has 3 components. t_n is the normal traction component, and t_s and t_t represent the two shear traction components. The corresponding normal and two shear components of the separation vector $\boldsymbol{\delta}$ are δ_n, δ_s and δ_t, respectively. **K** represents the stiffness tensor connecting $\boldsymbol{t}$ and $\boldsymbol{\delta}$ before damage sets in as described in the 2D case. K_{nn}, K_{ss}, and K_{tt} are assumed to take the same value. Damage sets in when

$$\left\{ \left(\frac{t_n}{t_n^{\max}}\right)^2 + \left(\frac{t_s}{t_s^{\max}}\right)^2 + \left(\frac{t_t}{t_t^{\max}}\right)^2 \right\} = 1. \tag{B.2}$$

The maximum cohesive strength is assumed to be the same in the normal and two shear directions (partly owing to the lack of detailed experimental information) and is denoted as

$$T_{\max} = t_n^{\max} = t_s^{\max} = t_t^{\max}. \tag{B.3}$$

Since the normal and tangential strengths equal, the damage initiation criterion can simply be written as,

$$\frac{t}{T_{\max}} = \left\{ \frac{t_n^2 + t_s^2 + t_t^2}{T_{\max}^2} \right\}^{1/2} = 1. \tag{B.4}$$

In the above relation, t is the effective traction. When the effective separation ($\delta_m = \sqrt{\delta_n^2 + \delta_s^2 + \delta_t^2}$) reaches a value of δ_m^0, damage initiates, as shown in Fig. 8(a). The evolution of damage follows Eq. (23). The dependence of $T_{\max}$ on GB misorientation angle follows Eq. (25). The parameters used in the 3D model are given in Table B.1.

Table B.1
Parameters of the 3D traction separation law.

Q	K_{nn} (MPa)	$(\Phi_0)_{\max}$(kJ/mm^2)	T_G(MPa)	$T_{GB}^{\min}$(MPa)
1.5	500×10^6	1	962.5	641.67

References

Arafin, M.A., Szpunar, J.A., 2010. Modeling of grain boundary character reconstruction and predicting intergranular fracture susceptibility of textured and random polycrystalline materials. Comput. Mater. Sci. 50, 656–665.
Asaro, R.J., 1983. Micromechanics of Crystals and Polycrystals. In: Hutchinson, J.W., Wu, T.Y. (Eds.), Advances in Applied Mechanics. Elsevier, pp. 1–115.
Asaro, R.J., Needleman, A., 1984. Flow localization in strain hardening crystalline solids. Scr. Metall. 18, 429–435.
Asaro, R.J., Rice, J., 1977. Strain localization in ductile single crystals. J. Mech. Phys. Solids 25, 309–338.
Bachurin, D., 2018. Influence of grain boundary misorientation on intergranular fracture of nanocrystalline palladium. Int. J. Fract. 214, 69–78.
Bond, D.M., Zikry, M.A., 2018. Differentiating between intergranular and transgranular fracture in polycrystalline aggregates. J. Mater. Sci. 53, 5786–5798.
Chen, C., Kolednik, O., Scheider, I., Siegmund, T., Tatschl, A., Fischer, F., 2003. On the determination of the cohesive zone parameters for the modeling of micro-ductile crack growth in thick specimens. Int. j. fract. 120, 517–536.
Chen, C., Wang, S., Jia, Y., Wang, M., Li, Z., Wang, Z., 2013. The orientation dependence of hot deformation behaviors of Mo with elongated grains. Int. J. Refract. Metals Hard Mater. 41, 603–608.
Chen, C., Wang, S., Jia, Y., Wang, M., Li, Z., Wang, Z., 2014. The effect of texture and microstructure on the properties of Mo bars. Mater. Sci. Eng A 601, 131–138.
Chen, H., Jiao, Y., Liu, Y., 2015. Investigating the microstructural effect on elastic and fracture behavior of polycrystals using a nonlocal lattice particle model. Mater. Sci. Eng. A 631, 173–180.
Chew, H.B., Hong, S., Kim, K.-S., 2009. Cohesive zone laws for void growth — II. numerical field projection of elasto-plastic fracture processes with vapor pressure. J. Mech. Phys. Solids 57, 1374–1390.
Choi†, S.T., Kim, K.S., 2007. Nanoscale planar field projections of atomic decohesion and slip in crystalline solids. part I. a crack-tip cohesive zone. Philos. Mag. 87, 1889–1919.
Christman, T., Needleman, A., Nutt, S., Suresh, S., 1989. On microstructural evolution and micromechanical modelling of deformation of a whisker-reinforced metal-matrix composite. Mater. Sci. Eng A 107, 49–61.
Clayton, J.D., Knap, J., 2016. Phase field modeling and simulation of coupled fracture and twinning in single crystals and polycrystals. Comput. Methods Appl. Mech. Eng. 312, 447–467.
Deve, H., Asaro, R., 1989. The development of plastic failure modes in crystalline materials: shear bands in FCC polycrystals. Metall. Trans. A 20, 579–593.
Featherston, F.H., Neighbours, J., 1963. Elastic constants of tantalum, tungsten, and molybdenum. Phys. Rev. 130, 1324.
Fuchs, P., Major, Z., 2011. Experimental determination of cohesive zone models for epoxy composites. Exp. Mech. 51, 779–786.
Ghosh, A., Patra, S., Chatterjee, A., Chakrabarti, D, 2016. Effect of local crystallographic texture on the fissure formation during Charpy impact testing of low-carbon steel. Metall. Mater. Trans. A 47, 2755–2772.
Gröger, R., Vitek, V., 2009. Temperature and strain rate dependent flow criterion for bcc transition metals based on atomistic analysis of dislocation glide. Int. J. Mater. Res. 100, 315–321.
Hill, R., Rice, J., 1972. Constitutive analysis of elastic-plastic crystals at arbitrary strain. J. Mech. Phys. Solids 20, 401–413.

Hong, S., Chew, H.B., Kim, K.-.S., 2009. Cohesive-zone laws for void growth — I. experimental field projection of crack-tip crazing in glassy polymers. J. Mech. Phys. Solids 57, 1357–1373.
Hong, S., Kim, K.-.S., 2003. Extraction of cohesive-zone laws from elastic far-fields of a cohesive crack tip: a field projection method. J. Mech. Phys. Solids 51, 1267–1286.
Kim, J.-.Y., Greer, J.R., 2008. Size-dependent mechanical properties of molybdenum nanopillars. Appl. Phys. Lett. 93, 101916.
Kim, J.-.Y., Jang, D., Greer, J.R., 2010. Tensile and compressive behavior of tungsten, molybdenum, tantalum and niobium at the nanoscale. Acta Mater. 58, 2355–2363.
Kim, J.-.Y., Jang, D., Greer, J.R., 2012. Crystallographic orientation and size dependence of tension–compression asymmetry in molybdenum nano-pillars. Int. J. Plast. 28, 46–52.
Kim, M.-.C., Jun Oh, Y., Hwa Hong, J., 2000. Characterization of boundaries and determination of effective grain size in Mn-Mo-Ni low alloy steel from the view of misorientation. Scr. Mater. 43, 205–211.
Kim, S., Lee, S., Lee, B.S., 2003. Effects of grain size on fracture toughness in transition temperature region of Mn–Mo–Ni low-alloy steels. Mater. Sci. Eng. A 359, 198–209.
Kobayashi, S., Inomata, T., Kobayashi, H., Tsurekawa, S., Watanabe, T., 2008. Effects of grain boundary-and triple junction-character on intergranular fatigue crack nucleation in polycrystalline aluminum. J. Mater. Sci. 43, 3792–3799.
Kowalski, N., Delannay, L., Yan, P., Remacle, J.-.F., 2016. Finite element modeling of periodic polycrystalline aggregates with intergranular cracks. Int. J. Solids Struct. 90, 60–68.
Li, Y., McDowell, D., Zhou, M., 2014. A multiscale framework for predicting fracture toughness of polycrystalline metals. Mater. Perform. Charact. 3, 157–172.
Li, Y., Zhou, M., 2013a. Prediction of fracture toughness of ceramic composites as function of microstructure: I. numerical simulations. J. Mech. Phys. Solids 61, 472–488.
Li, Y., Zhou, M., 2013b. Prediction of fracturess toughness of ceramic composites as function of microstructure: II. analytical model. J. Mech. Phys. Solids 61, 489–503.
Li, Y., Zhou, M., 2018. Effect of competing mechanisms on fracture toughness of metals with ductile grain structures. Eng. Fract. Mech.
Lim, L., Watanabe, T., 1989. Grain boundary character distribution controlled toughness of polycrystals—A two-dimensional model. Scr. Metall. 23, 489–494.
Lim, L., Watanabe, T., 1990. Fracture toughness and brittle-ductile transition controlled by grain boundary character distribution (GBCD) in polycrystals. Acta Metall. et Mater. 38, 2507–2516.
Lobanov, M., Danilov, S., Pastukhov, V., Averin, S., Khrunyk, Y., Popov, A., 2016. The crystallographic relationship of molybdenum textures after hot rolling and recrystallization. Mater. Des. 109, 251–255.
McGinty, R.D., McDowell, D.L., 2004. Application of multiscale crystal plasticity models to forming limit diagrams. J. Eng. Mater. Technol. 126, 285–291.
McHugh, P.E., Varias, A.G., Asaro, R.J., Shih, C.F., 1989. Computational modeling of microstructures. Future Gener. Comput. Syst. 5, 295–318.
Molkeri, A., Srivastava, A., Osovski, S., Needleman, A., 2019. Influence of grain size distribution on ductile intergranular crack growth resistance. J. Appl. Mech. 1–11.
Needleman, A., 1992. Micromechanical modelling of interfacial decohesion. Ultramicroscopy 40, 203–214.
Needleman, A., 1993. Size Effects in the Analysis of Ductility Under Dynamic Loading Conditions, 180. Asme Applied Mechanics Division-Publications-AMD, p. 55. -55.
Nolze, G., Hielscher, R., 2016. IPF Coloring of Crystal Orientation Data. Universität Chemnitz. Preprint Technische.
Oertel, C.-.G., Hünsche, I., Skrotzki, W., Lorich, A., Knabl, W., Resch, J., Trenkwalder, T., 2010. Influence of cross rolling and heat treatment on texture and forming properties of molybdenum sheets. Int. J. Refract. Metals Hard Mater. 28, 722–727.
Peirce, D., Asaro, R., Needleman, A., 1982. An analysis of nonuniform and localized deformation in ductile single crystals. Acta Metall. 30, 1087–1119.
Peirce, D., Asaro, R.J., Needleman, A., 1983. Material rate dependence and localized deformation in crystalline solids. Acta Metall. 31, 1951–1976.
Povirk, G.L., Nutt, S.R., Needleman, A., 1992. Analysis of creep in thermally cycled Al/SiC composites. Scr. Metall. et Mater. 26, 461–466.
Prakash, C., Gunduz, I.E., Oskay, C., Tomar, V., 2018. Effect of interface chemistry and strain rate on particle-matrix delamination in an energetic material. Eng. Fract. Mech. 191, 46–64.
Primig, S., Clemens, H., Knabl, W., Lorich, A., Stickler, R., 2015. Orientation dependent recovery and recrystallization behavior of hot-rolled molybdenum. Int. J. Refract. Metals Hard Mater. 48, 179–186.
Rice, J.R., 1968. A path independent integral and the approximate analysis of strain concentration by notches and cracks. J. Appl. Mech. 35, 379–386.
Roy, U., Zhou, M., 2020. A computational framework for predicting the fracture toughness of metals as function of microstructure. J. Mech. Phys. Solids 142, 103955.
Sham, T.L., Needleman, A., 1983. Effects of triaxial stressing on creep cavitation of grain boundaries. Acta Metall. 31, 919–926.
Simonovski, I., Cizelj, L., 2015. Cohesive zone modeling of intergranular cracking in polycrystalline aggregates. Nucl. Eng. Des. 283, 139–147.
Sisodia, P., Verma, M., 1990. Polycrystalline elastic moduli of some hexagonal and tetragonal materials. Phys. Status Solidi (A) 122, 525–534.
Sørensen, B.F., Jacobsen, T.K., 2003. Determination of cohesive laws by the J integral approach. Eng. Fract. Mech. 70, 1841–1858.
Sreeramulu, K., Sharma, P., Narasimhan, R., Mishra, R.K., 2010. Numerical simulations of crack tip fields in polycrystalline plastic solids. Eng. Fract. Mech. 77, 1253–1274.
Standard, A., 2001. Standard Test Method for Measurement of Fracture Toughness. ASTM, pp. 1–46. E1820-01.
Sturm, D., Heilmaier, M., Schneibel, J.H., Jéhanno, P., Skrotzki, B., Saage, H., 2007. The influence of silicon on the strength and fracture toughness of molybdenum. Mater. Sci. Eng A 463, 107–114.
Taylor, G.I., 1938. Plastic strain in metals. J. Inst. Metals 62, 307–324.
Tomar, V., Zhai, J., Zhou, M., 2004. Bounds for element size in a variable stiffness cohesive finite element model. Int. J. Numer. Methods Eng. 61, 1894–1920.
Watanabe, T., 1993. Grain boundary design and control for high temperature materials. Mater. Sci. Eng A 166, 11–28.
Watanabe, T., 1994. The impact of grain boundary character distribution on fracture in polycrystals. Mater. Sci. Eng A 176, 39–49.
Watanabe, T., 2011. Grain boundary engineering: historical perspective and future prospects. J. Mater. Sci. 46, 4095–4115.
Watanabe, T., Tsurekawa, S., 1999. The control of brittleness and development of desirable mechanical properties in polycrystalline systems by grain boundary engineering. Acta Mater. 47, 4171–4185.
Welch, P., Davies, G., 1983. Texture and cleavage in molybdenum. Texture Stress Microstruct. 6, 21–37.
Wilson, D., Zheng, Z., Dunne, F.P.E., 2018. A microstructure-sensitive driving force for crack growth. J. Mech. Phys. Solids 121, 147–174.
Xu, X.-.P., Needleman, A., 1994. Numerical simulations of fast crack growth in brittle solids. J. Mech. Phys. Solids 42, 1397–1434.
Xu, X.-.P., Needleman, A., 1996. Numerical simulations of dynamic crack growth along an interface. Int. J. Fract. 74, 289–324.
Zikry, M., 1992. Failure Modes in Cubic Crystalline Materials, 36. ASME-PUBLICATIONS-AD, p. 199. -199.
Zikry, M.A., Kameda, T., 1998. Inelastic three dimensional high strain-rate dislocation density based analysis of grain-boundary effects and failure modes in ordered intermetallics. Mech. Mater. 28, 93–102.
Zikry, M.A., Kao, M., 1995. Large-scale crystal plasticity computations of microstructural failure modes. Comput. Syst. Eng. 6, 225–240.
Zikry, M.A., Kao, M., 1996. Inelastic microstructural failure mechanisms in crystalline materials with high angle grain boundaries. J. Mech. Phys. Solids 44, 1765–1798.